External Influences on Modeled and Observed Cloud Trends

KATE MARVEL

Lawrence Livermore National Laboratory, Livermore, California, and NASA Goddard Institute for Space Studies, and Department of Applied Physics and Applied Mathematics, Columbia University, New York, New York

MARK ZELINKA, STEPHEN A. KLEIN, CÉLINE BONFILS, PETER CALDWELL, CHARLES DOUTRIAUX, BENJAMIN D. SANTER, AND KARL E. TAYLOR

Lawrence Livermore National Laboratory, Livermore, California

(Manuscript received 29 October 2014, in final form 3 February 2015)

ABSTRACT

Understanding the cloud response to external forcing is a major challenge for climate science. This crucial goal is complicated by intermodel differences in simulating present and future cloud cover and by observational uncertainty. This is the first formal detection and attribution study of cloud changes over the satellite era. Presented herein are CMIP5 model-derived fingerprints of externally forced changes to three cloud properties: the latitudes at which the zonally averaged total cloud fraction (CLT) is maximized or minimized, the zonal average CLT at these latitudes, and the height of high clouds at these latitudes. By considering simultaneous changes in all three properties, the authors define a coherent multivariate fingerprint of cloud response to external forcing and use models from phase 5 of CMIP (CMIP5) to calculate the average time to detect these changes. It is found that given perfect satellite cloud observations beginning in 1983, the models indicate that a detectable multivariate signal should have already emerged. A search is then made for signals of external forcing in two observational datasets: ISCCP and PATMOS-x. The datasets are both found to show a poleward migration of the zonal CLT pattern that is incompatible with forced CMIP5 models. Nevertheless, a detectable multivariate signal is predicted by models over the PATMOS-x time period and is indeed present in the dataset. Despite persistent observational uncertainties, these results present a strong case for continued efforts to improve these existing satellite observations, in addition to planning for new missions.

1. Introduction

Because of the widely varying radiative feedbacks that they induce (Andrews et al. 2012; Bony et al. 2006; Stephens 2005; Vial et al. 2013), the responses of clouds to a warming planet represent the largest source of uncertainty in model projections of future climate change. An abiding goal of climate science is to evaluate the cloud changes simulated by models against those that have occurred in nature to determine whether models have a basis in reality and whether the human influence on cloud properties is discernable in observations. However, the relative magnitudes of forced and unforced cloud changes on the time scales allowed by the observed record have yet to be systematically quantified. Achieving this goal is difficult because a long, reliable, bias-free, and artifact-free record of cloud properties does not exist, as most long-term cloud records are plagued by spurious trends arising from various artifacts. Moreover, many of the robustly simulated cloud responses to external forcing can also arise as a result of natural climate variability alone, with the magnitude of the unforced response relative to the forced response increasing as shorter time scales are considered. Nevertheless, models project robust climate changes that are likely to affect large-scale cloud properties: poleward shifts of key atmospheric circulation features (Yin 2005), an intensification of the hydrological cycle (Held and Soden 2006), and changes to the vertical temperature structure (Santer et al. 2003, 2013). In this study we use these properties to perform the

Corresponding author address: Kate Marvel, NASA Goddard Institute for Space Studies and Department of Applied Physics and Applied Mathematics, Columbia University, 2880 Broadway, New York, NY 10025.
E-mail: katherine.d.marvel@nasa.gov

DOI: 10.1175/JCLI-D-14-00734.1

© 2015 American Meteorological Society

first formal detection and attribution study on observed cloud trends. This requires that we first consider a number of related questions:

- Can we identify the fingerprints of external forcing on model cloud properties, and if so, are they distinct from patterns that arise from internal variability alone?
- How long an observational record is theoretically required to ensure detection of an externally forced signal above the noisy background of natural climate variability?
- Does a multivariate fingerprint that encompasses coherent changes in multiple cloud properties present advantages over a fingerprint tracking changes in a single variable?
- How strongly are the fingerprints of external forcing agents expressed in two long-term satellite records?

To answer these questions, we first define indicators that track features of interest in modeled cloud fields (section 2). These indicators are then used in section 3 to derive fingerprints of externally forced cloud changes that characterize the robustly simulated coherent response of three relevant cloud properties to external forcing. In section 4 we quantify the strength of the "signal" of externally forced cloud changes and the "noise" arising from natural cloud variability in models, and determine in section 5 the year in which the multimodel average signal of externally forced cloud change emerges, along with the uncertainty in this estimate. Finally, in section 6, we perform a formal detection and attribution of the externally forced fingerprint in the observational cloud record.

2. Cloud change indicators used in this study

In this study, we rely both on observations and on model results from phase 5 of the Coupled Model Intercomparison Project (CMIP5). We make use of unforced preindustrial control (piControl) simulations and historical simulations extended to 2100 by splicing with the appropriate representative concentration pathway 8.5 (RCP8.5) simulation (ALL+8.5). Further details of the models used are given in appendix A.

To detect and track coherent changes across multiple models, we require indicators that can identify robust physical processes even in the presence of model errors and biases. Marvel and Bonfils (2013) introduced a method to simultaneously track changes in the location and intensity of major precipitation features. Here, we build on these techniques to introduce three simple indicators of cloud change, which we will use to detect changes in the latitude **L** of the cloudiest and clearest regions, the total cloud amount **C** in these regions, and the height **H** of high clouds.

a. *CLT-derived indicators:* **L** *and* **C**

Latitude and cloudiness indicators are derived from boreal winter [December–February (DJF)] mean total cloud fraction (CLT; Fig. 1a). There are several reasons for restricting our analysis to DJF averages; these are discussed in section 3. In almost all CMIP5 ALL+8.5 and piControl simulations, there are exactly five local extrema in the smoothed CLT field: maxima over the tropics and midlatitude storm tracks, and minima in the subtropical dry zones. We do not consider models for which this is not true in the 1980–2005 climatology, as described in section 2. Our method identifies the latitudes and cloud amounts at these five locations to define two time-varying indicators. For every year that every month in DJF is available, we analyze the data as follows:

1) Zonally average the total cloud fraction.
2) Apply a Gaussian filter with width 5° latitude to the zonal average.
3) Use a peak-finding algorithm to determine the local extrema (Fig. 1b).
4) For most models, there are exactly two local minima and three local maxima for every year's DJF average. The latitudes at which these extrema occur are recorded, as are the values of the smoothed CLT. These will form the basis for our **L** and **C** indicators, respectively.
5) In the rare (fewer than 3.4% of model years in the ALL+8.5 simulations) cases for which there are more or fewer local extrema than anticipated, missing values are returned at all five extrema in that year. In subsequent fingerprinting and projection, if any value is missing in a model at a given year, the model does not contribute to the multimodel average (MMA) at that time. Figure 2 shows that when the analysis is restricted to DJF, there is no discernible trend in the fraction of models that contribute to the MMA over time.

The resulting MMA time series, measuring the latitudes and total cloud fraction at these local extrema, are both of dimension $n_T \times 5$, where n_T is the analysis length.

We define the **L** and **C** indicators as the anomalies of the resulting latitude and total cloud fraction time series, respectively. Anomalies are calculated on a model-by-model basis with respect to the 1983–2007 time average (in the spliced ALL+8.5 runs and the observations) or the 200-yr climatology (for piControl simulations).

b. *CL-derived indicator:* **H**

Our height indicator **H** is constructed from the three-dimensional cloud fraction (CL; Fig. 1c). As with CLT, we consider DJF averages. For every year, we calculate the **H** indicator as follows:

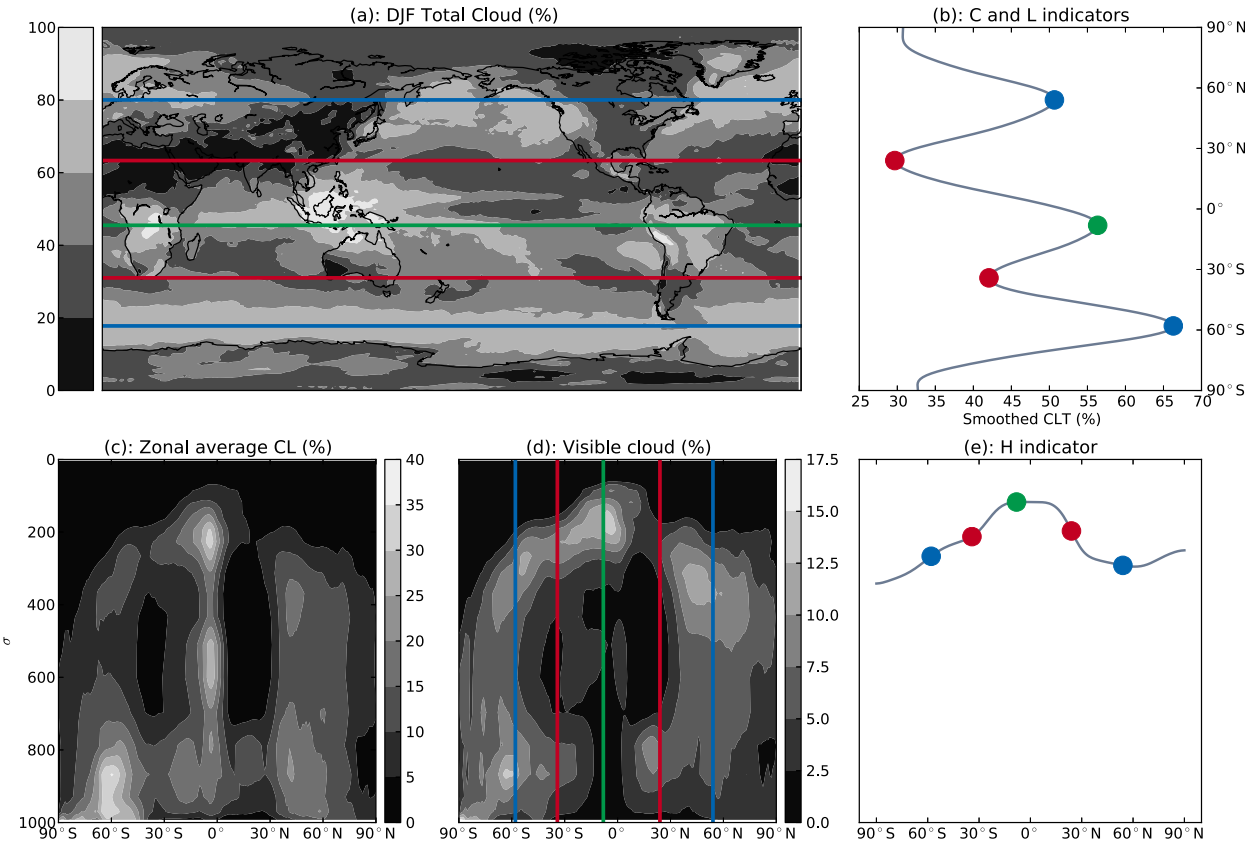

FIG. 1. Cloud indicators used in this study, illustrated using the cloud fraction from a representative climate model (CCSM4) in DJF of year 2000. (a) Total cloud fraction is first (b) zonally averaged and smoothed. The **L** and **C** indicators measure the latitude and smoothed total cloud fraction, respectively, of the five local extrema in the smoothed zonal average [filled circles in (b)]. (c) Starting with the cloud fraction on model vertical levels (σ; hPa), we calculate (d) the nonoverlapped cloud fraction that is visible to space, and then obtain (e) the weighted cloud-top pressure for clouds above the 440-hPa level. The **H** indicator is the value of weighted cloud-top pressure at each of the five latitudes [filled circles in (e)].

1) To emulate what a satellite might see, we estimate the cloud fraction at each vertical level that is visible from space $\mathrm{CL}^{(\mathrm{visible})}$ assuming random overlap (Tian and Curry 1989). This step is illustrated in Fig. 1d.
2) We compute each model's temporally and spatially varying pressure field on the native grid levels upon which CL is defined.
3) For each grid box, we determine the index of the lowest native grid level ℓ such that the pressure at the lower boundary of the cell $P(\ell) < 440\,\mathrm{hPa}$. This is the standard ISCCP criterion for high cloud.
4) Three-dimensional model cloud fields are reported on pressure levels that vary spatially, temporally, and across models. We therefore require a step to determine model CL at the bottommost level closest to 440 hPa. Assuming that $P(\ell)$ decreases with increasing ℓ, we interpolate between the levels just above and just below 440 hPa (ℓ and $\ell - 1$) as follows:

$$A = \frac{440\,\mathrm{hPa} - P(\ell)}{P(\ell-1) - P(\ell)},$$

$$\mathrm{CL}^{(\mathrm{visible})}_{\mathrm{bottom}} = A \times \mathrm{CL}^{(\mathrm{visible})}(\ell - 1), \quad \text{and}$$

$$P_{\mathrm{bottom}} = \frac{P(\ell) + 440\,\mathrm{hPa}}{2}.$$

5) To measure the altitude of high clouds, we calculate the weighted cloud-top pressure (WCTP) at every grid cell, defined as

$$\mathrm{WCTP} = \frac{\left[\sum_{i=\ell}^{\ell_0} \mathrm{CL}^{(\mathrm{visible})}(i)P(i)\right] + \mathrm{CL}^{(\mathrm{visible})}_{\mathrm{bottom}} P_{\mathrm{bottom}}}{\sum_{i=\ell}^{\ell_0} \mathrm{CL}^{(\mathrm{visible})}(i) + \mathrm{CL}^{(\mathrm{visible})}_{\mathrm{bottom}}}. \tag{1}$$

Here, ℓ_0 is the highest vertical level in the model.
6) We zonally average the resulting WCTP.
7) We spatially smooth the zonal average WCTP with the same Gaussian filter applied to the CLT-derived indicators (**L** and **C**).

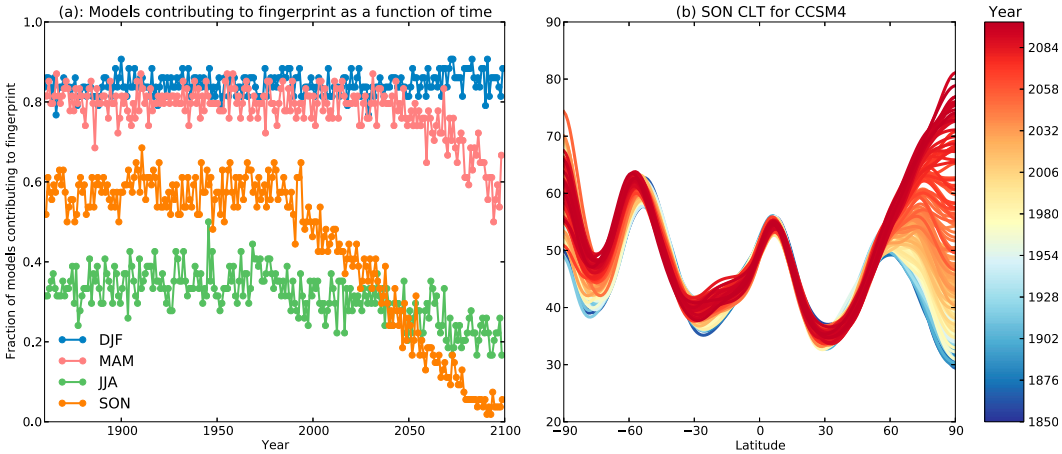

FIG. 2. (a) Fraction of models with all five CLT extrema present as a function of time. In July–August (JJA), less than half the models contain five distinct extrema in the smoothed zonal average CLT. In September–November (SON) and March–May (MAM), most models have five extrema in the earlier part of the record, but the number of models with five extrema decreases with time. (b) Boreal autumn (SON) average CLT for a representative model (CCSM4). Initially, five CLT extrema are detected, but with time, the northern polar cloud fraction increases so much that the NH peak corresponding to the storm track ceases to exist.

8) Having previously calculated **L**, we determine the WCTP at each of the five latitudes that correspond to local extrema in CLT at the time step in question.
9) The **H** indicator at time t is the WCTP at each of the five latitudes multiplied by -1, such that a decrease in WCTP, which corresponds to an increase in cloud height, leads to a positive change in **H**.

The result is a time series of dimension $n_T \times 5$ representing the WCTP at the cloudiest and clearest latitudes. As for **L** and **C**, the height indicator **H** is defined as an anomaly time series relative to the respective model climatology.

We note that several models have made use of the ISCCP simulator (Klein and Jakob 1999; Webb et al. 2001) to directly calculate output that is more similar to observations. Were we to make use of this output, we could eliminate the "visible cloud" calculation described in steps 1–4 above. However, because of the computational time required to implement the ISCCP simulator, relatively few models have done so: at the time of writing, only eight have contributed valid ISCCP simulator output to the CMIP5 piControl repository, seven to the historical repository, and none to the RCP8.5 repository. [Note that "valid" means that the simulator was implemented properly, which rules out the IPSL models; see Zelinka et al. (2013) for details.] Thus, to ensure a sufficiently large sample size in the multimodel archive, we rely instead on indicators derived from standard cloud diagnostics as described above.

c. *Further details*

1) ANOMALIES

It is well known that major features of the zonal circulation simulated by models are not always found at exactly the same latitudes (see, e.g., Levy et al. 2013, 2014; Scheff and Frierson 2012). This means that simply performing a multimodel average may blur or even eliminate boundaries between, for example, relatively cloudy and relatively clear latitudes.

The indicators for each simulation we consider are thus defined as anomalies relative to that particular simulation's climatology. Operating in this anomaly space is useful because models vary in their simulation of absolute values of cloud fraction, the latitudinal locations of **C** extrema, and the vertical distribution of clouds (Fig. 3). This strategy yields estimates of trends in **L**, **H**, and **H** that are less affected by model biases in the locations or intensity of major features, which may be substantial (Fig. 3). Marvel and Bonfils (2013) used similar methods to detect poleward shifts of the midlatitude storm tracks that are robust across multiple models, despite model errors in the locations of the storm tracks.

2) MODEL SELECTION

The "five extrema" structure identified in section 2a is physically motivated: we expect to see peaks in the tropics and midlatitudes associated with tropical convection and storm tracks, respectively. We also expect the dry subsidence regions in the subtropics to be relatively clear.

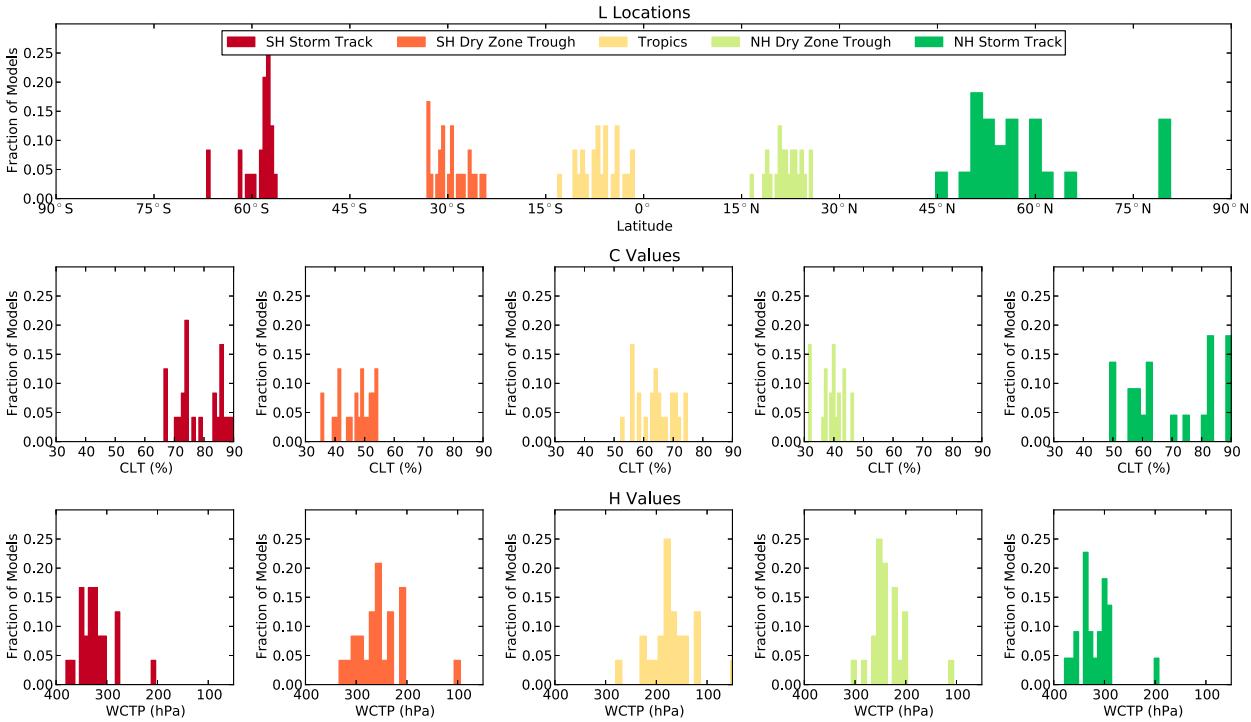

FIG. 3. Histograms of the climatological locations, obtained from CMIP5 preindustrial control simulations, of (top) total cloud fraction (CLT) extrema, (middle) values of smoothed CLT at these locations, and (bottom) weighted cloud-top pressures at these locations.

As we shall see in section 6, we also find this to be true for both observational datasets considered. The combination of physical expectation and presence in the observations leads us to define a five-extrema test for model simulations: if there are not exactly three maxima and two minima in a model's smoothed 1980–2005 zonal average DJF CLT climatology, we mask out (i.e., do not consider) all data from that model. All models, with the exception of the two NASA Goddard Institute for Space Studies models (GISS-E2-R and GISS-E2-H; see Table A1 for more information about individual models), pass this test.

As noted in point 5 of section 2a, we also mask individual model years in which the five-extrema test fails. This represents a more ad hoc model selection criterion, but because many simulations contain at least one year in which there are more than or fewer than five extrema, we judge it necessary to maintain a large sample size of models. We find no evidence that the years in which this test fails are not randomly distributed, and this results in our discarding fewer than 4% of model years in our analyses.

3) JUSTIFICATION FOR BOREAL WINTER

In this study, we confine our analysis to boreal winter. There are three reasons for this choice. First, there are exactly five local extrema at every time step in the observations and in most models for DJF. Both Northern and Southern Hemisphere storm tracks are apparent and detectable in boreal winter; the Northern Hemisphere (NH) storm tracks weaken in summer and will not necessarily be present as a local maximum in the zonal average CLT. In general, however, Southern Hemisphere (SH) storm tracks are detectable in all seasons. Second, the ISCCP dataset used relies on observations in the visible range and thus has no coverage over the very high latitudes in the winter hemisphere. In DJF, however, the NH storm tracks are sufficiently far south to be detectable.

Finally, considering the DJF average ensures that all five extrema are likely to be present in models over the entire observed time period; this is not the case for other seasons (Figs. 2a,b). In the RCP8.5 scenario, all models predict increasing global temperatures and associated loss of sea ice. In all seasons except boreal winter, the replacement of NH sea ice with open water results in large increases in total cloud fraction in the northern polar regions. This means that in later years the NH storm track is no longer detectable as a local extremum. Because our methodology masks out years in which fewer than five extrema are detected, this will spuriously weight earlier times in the MMA quantities.

d. *Indicator summary*

In summary, **L**, **C**, and **H** provide measures, respectively, of

1) where the cloudiest and clearest regions may be found in a particular model,
2) how cloudy these regions are, and
3) the altitude of high clouds in these regions.

These indicators are restricted to boreal winter and, being derived from zonal averages, fail to capture important cloud features that are nonzonal, particularly in northern latitudes. However, **L**, **C**, and **H** are computationally efficient to derive from a large ensemble of models and experiments, inherit many of the useful features described by Marvel and Bonfils (2013), and summarize key features of the global pattern of cloud cover that are highly relevant to cloud feedback.

3. Fingerprints

In the parlance of climate change detection and attribution (D&A), the "fingerprint" is the spatial pattern that characterizes the climate system response to external forcing (see, e.g., Allen and Stott 2003; Gillett et al. 2002; Hegerl et al. 1996; Stott et al. 2000; Tett et al. 2002). In this study, we use techniques developed and refined by, for instance, Barnett et al. (2008) and Santer et al. (1995, 2013). We calculate this pattern using the externally forced ALL+8.5 simulations spanning the period 1900–2100.

The multivariate fingerprint is calculated as follows.

1) For every ALL+8.5 simulation, we obtain time-varying indicators $\mathbf{L}^a$, $\mathbf{C}^a$, and $\mathbf{H}^a$ using the methods described in section 2. The superscript a indicates that these indicators are derived from ALL+8.5 spliced model simulations.
2) As we are constructing a fingerprint across multiple variables measured in different units, we require some means of removing dimensional information from the indicators. We therefore define normalized indicators $\mathbf{L}^a_{\mathrm{norm}}$, $\mathbf{C}^a_{\mathrm{norm}}$, and $\mathbf{H}^a_{\mathrm{norm}}$ by dividing through by the standard deviation of each indicator's time series at each location. This ensures that, for any $\mathbf{X} \in \{\mathbf{L}^a_{\mathrm{norm}}, \mathbf{C}^a_{\mathrm{norm}}, \mathbf{H}^a_{\mathrm{norm}}\}$, the matrix $\mathbf{X}^{\mathrm{T}}\mathbf{X}$ is a correlation rather than a covariance matrix. This has the effect of giving all five extrema (and all three indicators) equal weight in our subsequent EOF calculation.
3) We then average the ALL+8.5 indicators, first over an individual model's realizations if more than one is available, and then over all models to obtain MMA indicators $\overline{\mathbf{L}^a_{\mathrm{norm}}}$, $\overline{\mathbf{C}^a_{\mathrm{norm}}}$, and $\overline{\mathbf{H}^a_{\mathrm{norm}}}$. This double average over realizations and models effectively damps internal variability because manifestations of random natural phenomena such as ENSO are uncorrelated across models. It also effectively guards against a model with many realizations unduly influencing the mean.
4) We compute the joint correlation matrix $\mathbf{M}^{\mathrm{T}}\mathbf{M}$, where $\mathbf{M}$ is a 15-element vector made up of the three normalized indicators at five locations, averaged across all realizations and models:

$$\mathbf{M} = (\overline{\mathbf{L}^a_{\mathrm{norm}}}, \overline{\mathbf{C}^a_{\mathrm{norm}}}, \overline{\mathbf{H}^a_{\mathrm{norm}}}).$$

5) The multivariate climate change fingerprint (Santer et al. 1995) is then defined as the eigenfunction of $\mathbf{M}^{\mathrm{T}}\mathbf{M}$ corresponding to the largest eigenvalue (i.e., the leading EOF of $\mathbf{M}$).

The resulting multivariate fingerprint $F_m(L, C, H)$ is shown in Fig. 4a. This pattern is characterized by three robust physical processes that are consistently simulated in anthropogenically forced model experiments: poleward shifts of major climate zones (Wetherald and Manabe 1988; Zelinka et al. 2013; Bender et al. 2012), increases in midlatitudes and decreases in subtropics of total cloud fraction (evident here only in the Northern Hemisphere) (Zelinka et al. 2013), and a global rise in high cloud (Hansen et al. 1984; Hartmann and Larson 2002; Wetherald and Manabe 1988; Zelinka et al. 2013; Singh and O'Gorman 2012). The leading EOF explains over 91% of the variance in the MMA indicators.

Figure 4b, by contrast, shows the leading noise mode, defined as the leading EOF of the concatenated piControl indices (section 4b). One phase of this mode is characterized by an equatorward contraction of the major cloud features in the subtropics, and a rise of high cloud especially in the tropics and subtropics. This is unsurprising given that ENSO (the leading mode of internal variability in most models) is known to cause an equatorward contraction of the Hadley circulation (Lu et al. 2008), movement of the ITCZ (Deser and Wallace 1990), and a rise in tropical and subtropical high cloud tops (Zelinka and Hartmann 2011).

The fingerprint estimated from the ALL+8.5 runs is the response to combined anthropogenic and natural external forcing. The relative contributions to the fingerprint from purely natural changes in solar irradiance and volcanic aerosol loadings is therefore unclear in Fig. 4a. Previous D&A work illustrates that differences between the anthropogenic and ALL+8.5 fingerprints are relatively small over the satellite era [see, e.g., Fig. 2 in Santer et al. (2013)]. This suggests a relatively small natural contribution. The fingerprint obtained from the ALL+8.5 model simulations is very similar to that obtained from the multimodel ensemble average of model experiments in which atmospheric CO_2 is increased at 1% per year (Fig. 4c), indicating that the ALL+8.5

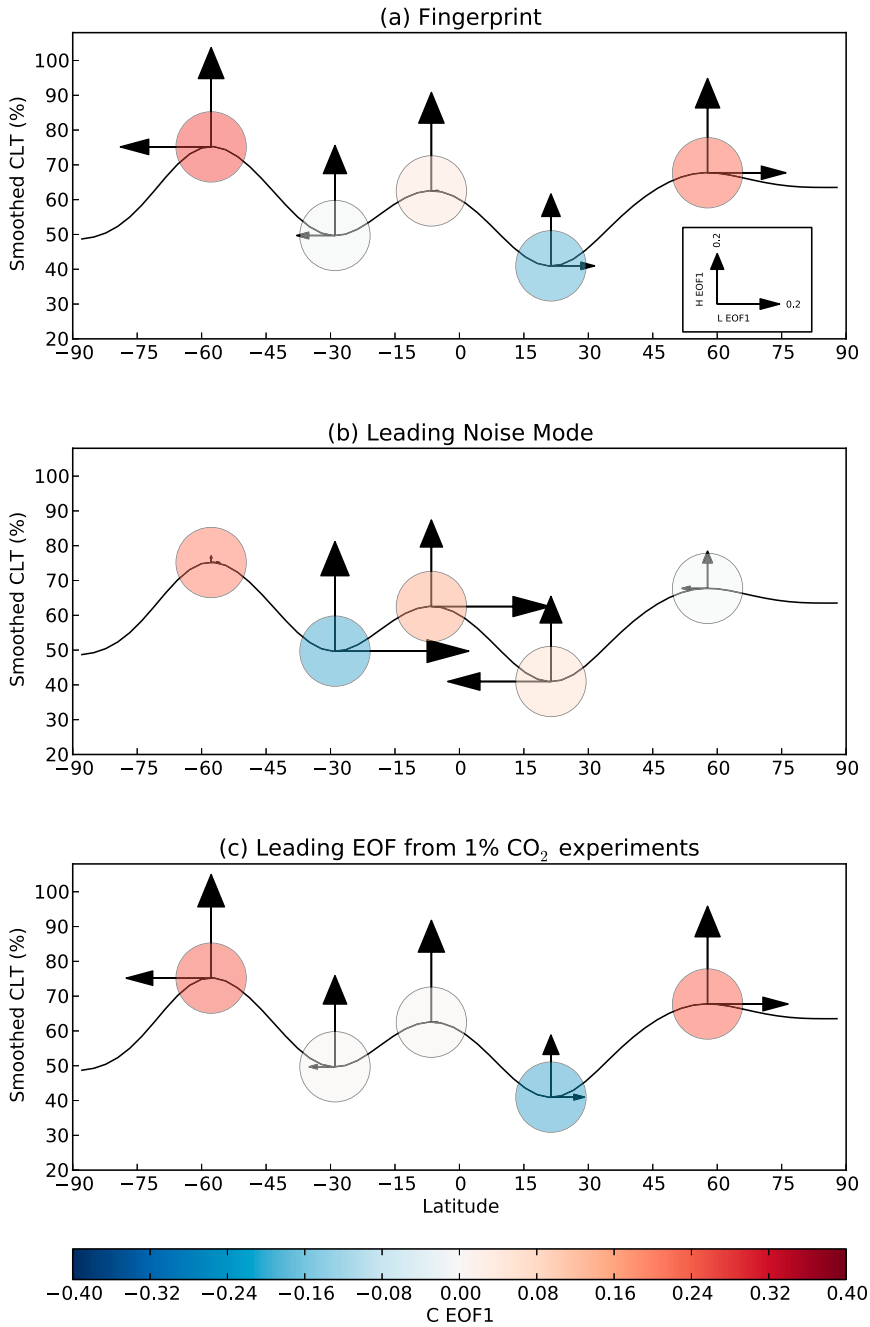

FIG. 4. (a) The multivariate fingerprint $F_m(L, C, H)$. The black curve shows, for illustrative purposes, the MMA piControl zonal average smoothed CLT. The L (H) components are represented as horizontal (vertical) arrows at each extremum of the smoothed CLT. The EOF loadings of L and H components are scaled according to the legend (bottom-right corner). The C components are represented as colored circles at the five extrema. (b) As in (a), but for the leading noise mode from concatenated control runs. (c) As in (a), but calculated from the multimodel average of CMIP5 1pctCO2 simulations.

fingerprint primarily reflects the response of clouds to anthropogenic changes in CO_2.

In subsequent sections, we will see that searching for coherent changes in the three indices simultaneously leads to earlier signal detection times. First, however, we consider the individual fingerprints of L, C, and H by calculating the correlation matrices of $\overline{\mathbf{L}^a_{\mathrm{norm}}}$, $\overline{\mathbf{C}^a_{\mathrm{norm}}}$, and $\overline{\mathbf{H}^a_{\mathrm{norm}}}$, respectively. The resulting five-element fingerprint for

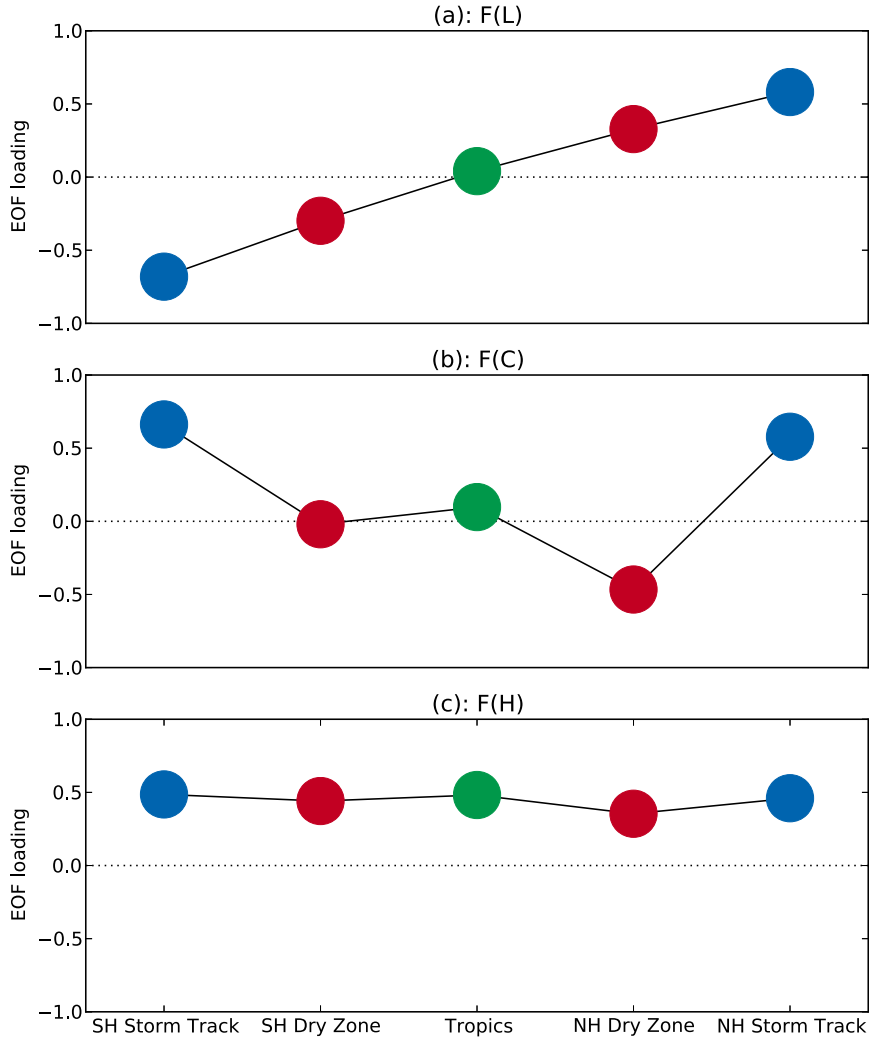

FIG. 5. Individual fingerprints (leading EOFs of the MMA correlation matrix) for the (a) latitude indicator **L**, (b) cloud amount indicator **C**, and (c) high cloud height indicator **H**.

each index is shown in Fig. 5. These patterns resemble their counterparts in the multivariate fingerprint $F_m(L, C, H)$. As expected, the latitude fingerprint $F(L)$ corresponds to poleward movement in both hemispheres. The cloudiness fingerprint $F(C)$ is described by clearing in the subtropical dry zones (albeit more in the Northern Hemisphere), little change in the tropics, and increasing cloudiness in the midlatitudes. The cloud height fingerprint $F(H)$ is characterized by a rise in high cloud at all latitudes considered.

4. Signal detection

a. Signal

The fingerprint F for some indicator or collection of indicators $\mathbf{X}$ is a function of location $\mathbf{x}$. Given suitably normalized observed or simulated data $O_{\mathbf{X}}(\mathbf{x}, t)$ with analysis length period n_T, the projection $P_{\mathbf{X}}(t) = \sum_{\mathbf{x}} O(\mathbf{x}, t) F(\mathbf{X}, \mathbf{x})$ provides a measure of the spatial covariance between the data and the fingerprint. If the data increasingly resemble the fingerprint, then the projection $P_{\mathbf{X}}(t)$ will trend upward with time. We define the signal of external forcing $S_{\mathbf{X}}(n_T)$ to be the slope of the best-fit line to $P_{\mathbf{X}}(t)$, obtained by least squares regression. This is a standard method commonly used in D&A research to detect signals of external forcing in observations (see, e.g., Barnett et al. 2008; Hasselmann 1979; Santer et al. 2007, 2013). The signal is, of course, a function of the analysis length n_T. In this paper, we calculate univariate signals, obtained by projecting any one indicator $\mathbf{X}$ onto its corresponding univariate fingerprint $F(\mathbf{X}, \mathbf{x})$, as well as the multivariate signal. The latter is calculated by constructing a 15-element vector from normalized observational or model data and projecting this vector onto the multivariate fingerprint $F_m(L, C, H)$.

b. Noise

How likely is a given signal to result from natural climate variability alone? To assess the significance of an observed signal, we require a null distribution of trends (i.e., information on the behavior of trends in pattern similarity between the fingerprint and natural internal variability). This distribution is constructed using natural internal variability estimates from the preindustrial control simulations. For each control run in the CMIP5 archive we derive latitude, cloudiness, and height indicators $\mathbf{L}^c$, $\mathbf{C}^c$, and $\mathbf{H}^c$ following the procedures described in section 2. Each indicator time series is divided by the temporal variance at each of the five extrema to obtain normalized indicators $\mathbf{L}^c_{\mathrm{norm}}$, $\mathbf{C}^c_{\mathrm{norm}}$, and $\mathbf{H}^c_{\mathrm{norm}}$. We then construct a time series of length 6800 years by concatenating each of the 34 control simulations (using only one control simulation per model). To prevent models with longer runs from dominating our calculation of internal noise, we use only the first 200 years of every model control simulation. By using multiple models with various amounts of noise, we might converge on a more realistic estimate (assuming no systematic error across models) of noise variability; we do not assume homogeneity of internal variability across all models. Moreover, including the first, rather than the last, 200 years of each simulation means that our noise estimate is likely to include long-term model drift, which may also result in a more conservative signal-to-noise estimate. It is these long piControl indicators that determine the leading noise mode shown in Fig. 4b.

We project these concatenated and normalized piControl indicators onto the univariate and multivariate fingerprints shown in Figs. 4a and 5. We then calculate the distribution of n_T-length trends in nonoverlapping segments of the resulting projection time series. This distribution is quasi-normal and distributed around zero, and its standard deviation $N_{\mathbf{X}}(n_T)$ provides a measure of internal climate variability, or noise. The value of $N_{\mathbf{X}}(n_T)$ will therefore vary with the analysis time scale n_T as well as the indicator $\mathbf{X}$ under consideration (Santer et al. 2013). Rather than recalculate noise on a model-by-model basis, we use the same noise estimate derived from the concatenated control runs for all models. This allows us to take advantage of the larger sample size that results from concatenation.

c. Signal-to-noise ratios

Dividing the univariate or multivariate signal $S_{\mathbf{X}}(n_T)$ by this noise measure yields the signal-to-noise ratio. If the signal-to-noise ratio exceeds (and remains above) 1.96, then we can claim to have detected a signal with 95% confidence relative to our best current multimodel estimates of natural internal variability. We use this two-tailed z test throughout to provide a conservative estimate of significance.

5. Detection times

When might we expect a detectable signal to emerge from the background of natural internal variability? Previous studies (see, e.g., Hawkins and Sutton 2012; Mahlstein et al. 2011) have recognized that, even in cases where the externally forced signal has not yet emerged from climate noise, there is still utility in calculating the "time of emergence" when it is predicted by models to do so. Unlike those studies, we focus not on regional patterns but on the global signal, defined as the projection onto a univariate or multivariate fingerprint. Our "detection time" is thus the time at which the global signal is predicted, in the MMA, to emerge from the noise.

The importance of trend detection for cloud studies was previously highlighted by Loeb et al. (2007), who calculate the time needed to detect a statistically significant trend in top-of-atmosphere flux assuming a statistical model (Weatherhead et al. 1998) for natural variability. Rather than rely on a statistical model, we instead use the piControl simulations in the CMIP5 archive for an estimate of internal variability. By treating individual ALL+8.5 simulations as equally plausible, we define the detection time (DT) (Santer et al. 2013) to be the year in which the signal-to-noise ratio for a model ALL+8.5 trend, beginning in 1983, exceeds and remains above the 95% significance threshold. The year 1983 is chosen because it is the first full year for which DJF satellite observations are available (section 6). The red line in Fig. 6 shows the MMA signal-to-noise ratio for the multivariate fingerprint. As expected, it increases with increasing trend length as trends in the models increasingly resemble the fingerprint while simultaneously becoming less and less likely to arise as a result of natural variability alone. The DT of the multivariate signal is 2010 in the MMA but ranges from 2001 to 2033 in individual simulations.

We then determine the signal-to-noise ratios for each univariate fingerprint and calculate the detection time for each indicator in isolation. Figure 6 illustrates the utility of the multivariate approach. The multimodel average H signal is strongest relative to internal noise (DT = 2026; individual models range between 2005 and 2050), while the MMA C and L signals emerge later in 2036 (2016–78 in individual models) and 2063 (from 1992 to later than 2100 in individual models), respectively. On average, a multivariate representation of signal and noise results in detection more than a decade earlier than would be expected from the strongest

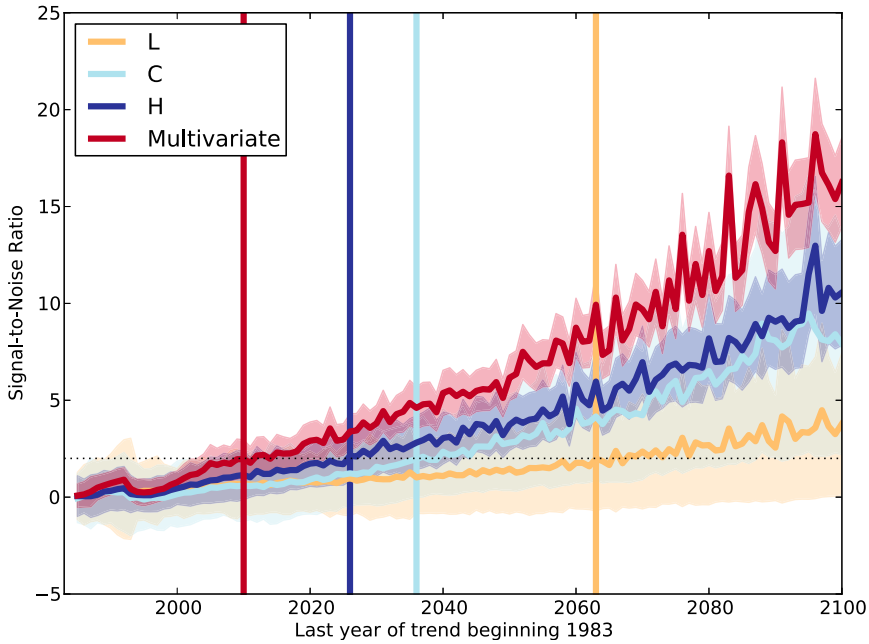

FIG. 6. Signal-to-noise ratio as a function of analysis length n_T. Solid lines represent the average of the multimodel signal-to-noise ratio; envelopes are ±2 intermodel standard deviations from the mean. Vertical lines show the MMA detection time.

single-variable detection time results, and five decades earlier than the L signal alone. The uncertainty in DT is also considerably reduced in the multivariate case, as the intermodel spread of L and C DTs exceeds a century but is only about 30 years for the multivariate DT.

6. Observations

In this section, we apply formal D&A methodology to satellite observations, using the two longest satellite-based records of global cloud properties available. The International Satellite Cloud Climatology Project dataset (ISCCP; Rossow and Schiffer 1999) covers the period July 1983 through June 2008, while the slightly longer Pathfinder Atmospheres–Extended dataset (PATMOS-x; Heidinger et al. 2012, 2014) spans the period January 1982 through December 2009. Both datasets have near-global coverage and provide independently retrieved estimates of total cloud fraction and its vertical distribution. Details of both datasets are provided in appendix B.

As discussed in the GEWEX Cloud Assessment (Stubenrauch et al. 2013), cloud retrievals from ISCCP and PATMOS-x are subject to errors and biases arising from numerous sources. For example, passive satellite retrievals can have difficulty distinguishing cloud from underlying cold and bright surfaces (Stubenrauch et al. 2013), and thus we expect considerable uncertainties in the observed high-latitude cloud properties in DJF. Moreover, numerous studies (e.g., Evan et al. 2007; Norris 1999, 2007) have identified potential sources of unphysical trends in existing observational datasets, including spurious drifts due to changes in satellite view angle and sensor calibration. For these reasons, the ISCCP and PATMOS-x datasets are not generally considered to be reliable for long-term trend analysis. In the following sections, we will show that, despite substantial observational uncertainty and known artifacts, useful trend information can be extracted from the existing observations.

a. Observational indicators

Observational $\mathbf{L}^o$ and $\mathbf{C}^o$ indicators are calculated from the ISCCP and PATMOS-x datasets as for the model data. We omit the random overlap calculation (step 2 in section 2b) in calculating the observed height indicator $\mathbf{H}^o(t)$ because the datasets already report visible cloud, and define weighted cloud-top pressure as

$$\mathrm{WCTP} = \frac{\sum_{i=5}^{7} \mathrm{CTP}_i \mathrm{CL}_i^{(\mathrm{visible})}}{\sum_{i=5}^{7} \mathrm{CL}_i^{(\mathrm{visible})}}. \tag{2}$$

Here, CTP is the observed cloud-top pressure. The sum is over pressure bins 5 through 7, which represent clouds at

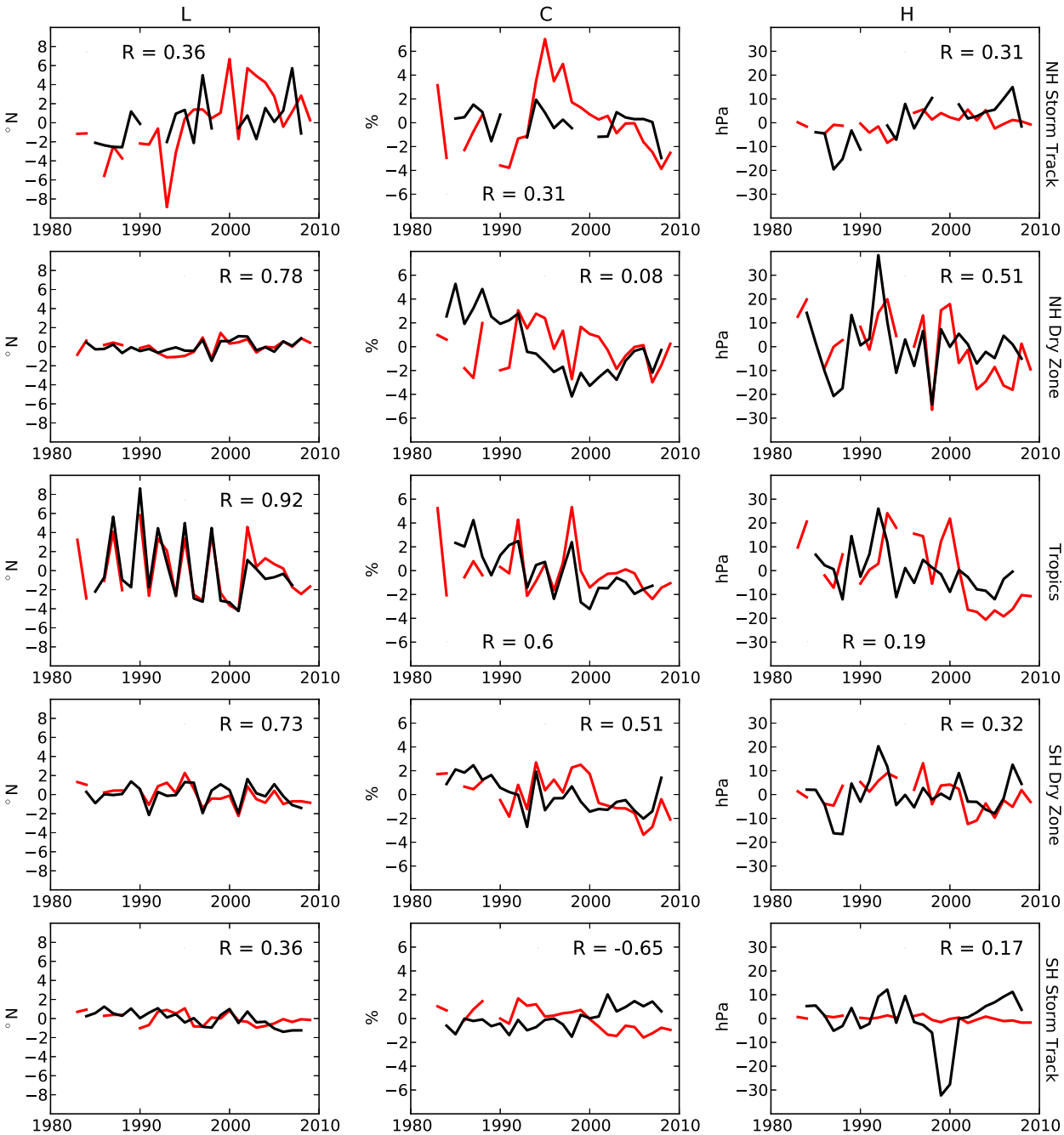

FIG. 7. The (left) **L**, (middle) **C**, and (right) **H** indicators for the ISCCP (black) and PATMOS-x (red) datasets. The correlation R between the observational datasets over the period 1984–2008 is indicated in each panel.

pressures below (altitudes above) 440 hPa, in keeping with the standard ISCCP high cloud classification. As in the model indicators described in section 2, the observational indicators $\mathbf{L}^o$, $\mathbf{C}^o$ and $\mathbf{H}^o$ are defined with respect to the climatology in the relevant observational dataset.

Figure 7 shows the resulting indicator time series, as well as the temporal correlation between the ISCCP and PATMOS-x datasets over the ISCCP analysis period. The correlations are largest in the latitude indicator, particularly in the tropics and subtropics. This suggests that that satellite records largely agree on trends in the locations of the cloudiest and clearest latitudes, and show the same temporal evolution. The same cannot be said of the cloud fraction at these latitudes. The observed cloudiness indicators $\mathbf{C}^o$ are weakly correlated (or even anticorrelated) at all locations, except at the tropical

peak. This makes it difficult to draw robust conclusions regarding total cloud fraction from the observations. There are likewise large differences in the mean weighted cloud-top pressure at all locations, and positive but small temporal correlations in the height indicator, with the weakest correlation found for the SH storm track. Thus, we identify consistency between observations in the **L** indicator, but not in the **C** or **H** indicators.

b. *Observed trends*

Figure 8 shows the observed and modeled trends for each indicator over the common period 1983–2007. Here, the indicators have not yet been normalized in order to report trends in physical units. At every location except the SH dry zone, both observational datasets agree with each other and with the MMA on the sign of the L trend. It is noticeable that the poleward migration of the storm tracks in both hemispheres is larger in ISCCP and PATMOS-x than in the model average, as seen in (Bender et al. 2012) for the models from phase 3 of CMIP (CMIP3). The sign of the C trends in the two observed datasets is in agreement in three of the five extrema, but differs in the storm tracks. The large ISCCP trend toward decreasing C in the tropics and subtropics is outside the range of model results, which may reflect temporal changes in satellite view angle (Norris 1999). The MMA trends in H indicate rising high clouds at all locations. While PATMOS-x shows large positive trends in cloud height at four of the five extrema, the height trend is within the model-predicted range only in the SH storm track. The ISCCP results, however, are even more inconsistent with the model predictions, and show an upward trend only in the tropics.

7. Detection and attribution results

By projecting suitably normalized observed **L**, **C**, and **H** indicators onto each of the individual-variable and multivariate fingerprints, we can measure the spatial similarity between the time-varying observations and the time-invariant model pattern of externally forced change. The observed signal is either the 27-yr PATMOS-x trend or the 25-yr ISCCP trend found in the projection time series. Because there are no observations of unforced natural variability, we rely on model piControl runs for our noise estimates. The observed signal-to-noise ratio for each indicator is therefore obtained by dividing the signal by the appropriate length noise term (section 4b), and this serves to normalize the indicators. Figures 9a–c show the projection of ISCCP and PATMOS-x **L**, **C**, and **H** indicators onto the individual normalized fingerprints $F(L)$, $F(C)$, and $F(H)$ (Fig. 5). Figure 9d shows the simultaneous projection of all three indicators onto the multivariate

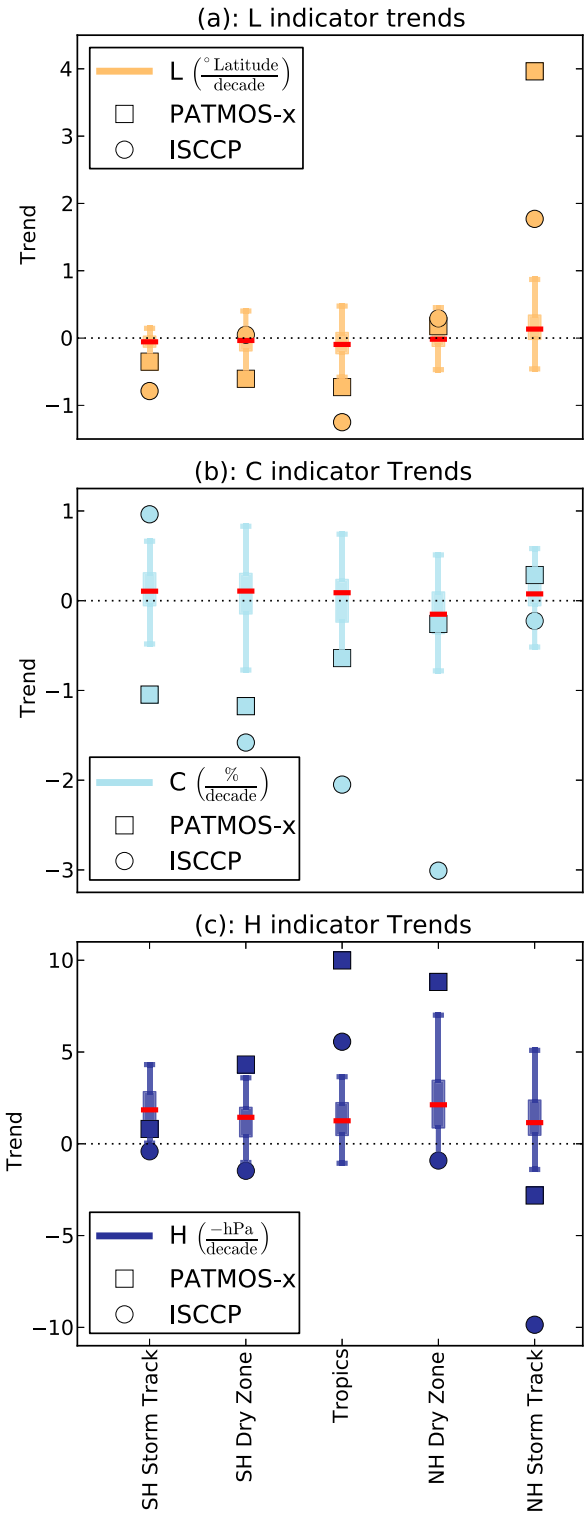

FIG. 8. The 1984–2008 trends in the (a) **L**, (b) **C**, and (c) **H** indicators in observed datasets [PATMOS-x (squares) and ISCCP (circles)]. The boxes in the box-and-whisker plots show the intermodel interquartile range (IQR) of the trends from historical runs for the recent historical period; red lines indicate the multimodel median. The whiskers show the range of model results after excluding outliers using the standard criteria of 1.5 times the IQR.

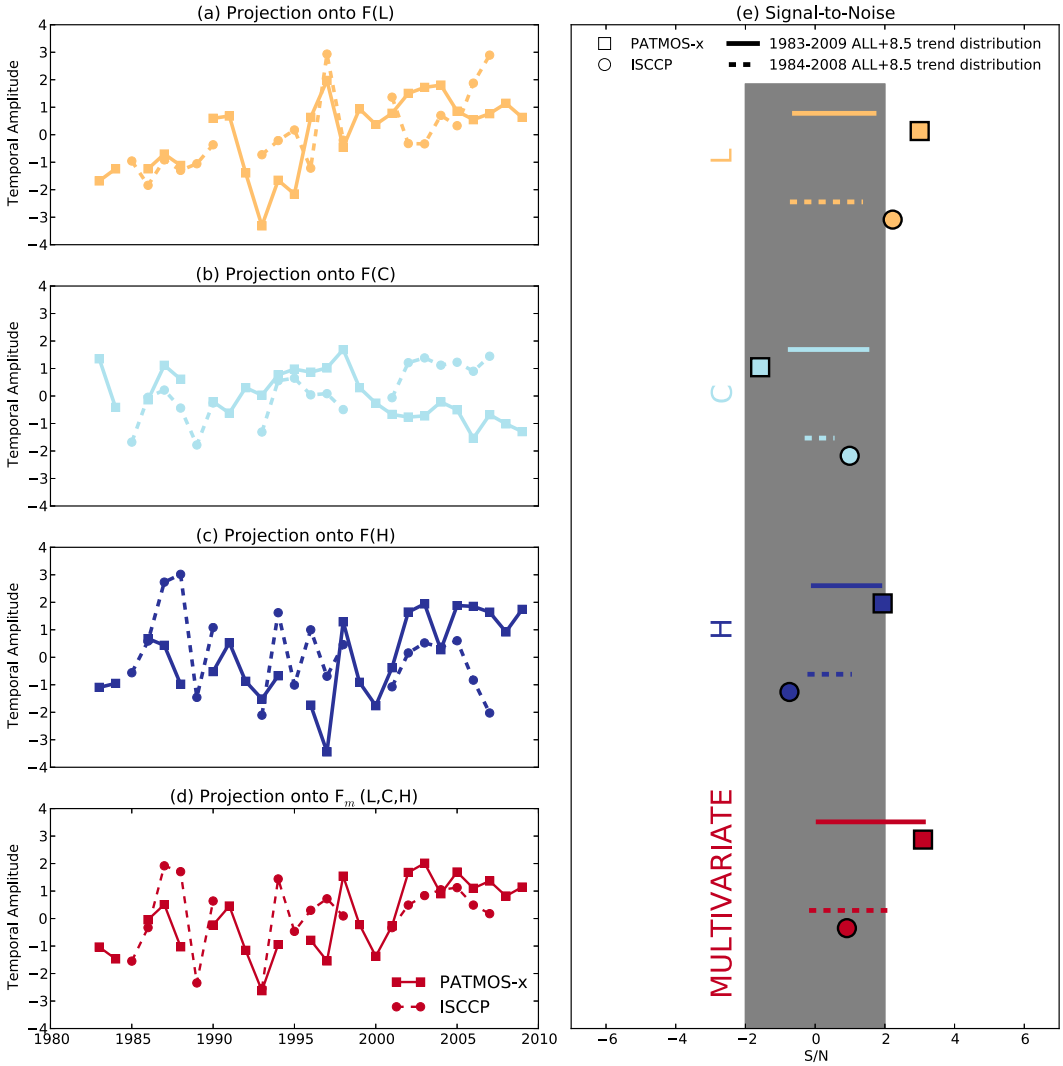

FIG. 9. (a)–(c) Projection of ISCCP (dashed lines with dots) and PATMOS-x (solid lines with squares) **L**, **C**, and **H** indicators onto the single-variable fingerprints $F(L)$, $F(C)$, and $F(H)$, respectively. (d) Multivariate projection of ISCCP and PATMOS-x indicators onto $F_m(L, C, H)$. (e) Modeled and observed signals, normalized by the relevant noise measure. Gray shading indicates ±1.96 noise standard deviations away from 0. Values that lie outside this envelope are incompatible with internal variability at 95% confidence. The 95% confidence intervals of ALL+8.5 trend distributions over the ISCCP (dashed) and PATMOS-x (solid) analysis periods are shown as horizontal lines. Observed trends are shown as squares (PATMOS-x) and circles (ISCCP).

fingerprint $F_m(L, C, H)$ (Fig. 4a). In Fig. 9e, we compare the observed signal-to-noise ratio to forced and piControl model signal-to-noise ratios. Model/observation comparisons are performed over the same time periods; also, to ensure accurate comparison between the models and observations, 27-yr forced trend distributions in Fig. 9e are calculated by masking (excluding data from) ALL+8.5 models in the years in which DJF PATMOS-x data are missing. Suitable noise distributions are calculated by masking the kth year in each 27-yr chunk of the concatenated piControl distribution, where k is the duration into the PATMOS-x record where data are missing.

In standard D&A methodology, an observed signal can be said to be detected at 95% confidence with a positive projection that lies more than 1.96 standard deviations away from the piControl distribution mean, a range indicated by the gray shading in Fig. 9e. If a detected signal lies within the distributions estimated from the individual ALL+8.5 models, it can reasonably be attributed to the collection of external forcings included in the historical and RCP8.5 simulations.

a. *Observed poleward migration incompatible with forced models*

Consistent with previous studies (Bender et al. 2012; Eastman et al. 2011), we find observational evidence for a poleward shift in the major features of the zonal CLT pattern. The L-only fingerprint $F(L)$ is increasingly apparent in both observational datasets and is incompatible with internal variability. However, it is also inconsistent with the 95% confidence interval of the ALL+8.5 model simulation. This is in agreement with previous studies that suggest models fail to capture the observed poleward expansion (Johanson and Fu 2009; Seidel et al. 2008). We note, however, that several authors have suggested that cloud shifts may not be trivially related to changes in the jet (Grise and Polvani 2014; Ceppi et al. 2014; Kay et al. 2014), and further study of the interaction between clouds and the circulation is necessary to understand this response.

b. *Observational uncertainty in total cloud fraction changes*

The observations disagree on trends in the projection onto $F(C)$, with PATMOS-x showing the amplitude of the cloudy-get-cloudier pattern decreasing and ISCCP showing it increasing. However, neither observed trend differs significantly from model-predicted noise. We note that the models do not predict a detectable signal in the C-only pattern over the ISCCP and PATMOS-x observational time periods.

c. *Observational uncertainty in high cloud changes*

Note that $F(H)$, in which high clouds rise everywhere, is increasingly strongly expressed in PATMOS-x but not in ISCCP. The PATMOS-x H-only signal is, in fact, on the cusp of detectability, although signal emergence is not predicted by the models. The 95% confidence levels of the ALL+8.5 forced model signal-to-noise distributions overlap the noise distributions, indicating that models do not predict a detectable signal over the PATMOS-x or ISCCP observational time periods.

d. *Multivariate signal detection in PATMOS-x*

Finally, both observational datasets show multivariate signals that overlap with the distribution of model externally forced results. The ISCCP multivariate signal is positive and compatible with ALL+8.5 models, but is not detectable above the noise background. We do not expect it to be so, however, as the ALL+8.5 trend distribution overlaps the noise distribution. In the PATMOS-x dataset, however, the multivariate signal is both compatible with ALL+8.5 model signals, but incompatible with natural variability at the 95% confidence level. Thus with PATMOS-x, the model-predicted multivariate fingerprint of cloud changes has been detected and attributed to external forcing. But this result should be interpreted with caution given the large discrepancies between observational datasets and the fact that the modeled distribution of forced signals overlaps substantially with the noise distribution. The overlap is consistent with the fact that the PATMOS-x record ends at the average multivariate model detection time, as determined in section 5.

8. Summary, discussion, and conclusions

Clouds are inherently noisy in space and time. Observational estimates of multidecadal cloud changes are relatively short and may contain spurious trends. However, in this study we have shown that the framework of climate change detection and attribution may be productively applied to both modeled and observed cloud properties.

Our results rely on new indicators to track simultaneous changes in three cloud properties: the latitudes at which the zonal average total cloud fraction reaches its maximum and minimum, the total cloud fraction at these cloudy and clear latitudes, and the height of high clouds at these latitudes. By tracking changes with respect to each model's climatology, the use of these indicators may partially eliminate complications that arise from model errors in the location or intensity of cloud features. Our indicators are defined at five spatial locations, a choice that restricts our analysis to boreal winter. Future work will consider annual means in the tropics and subtropics; our analysis suggests that observational uncertainty is highest in the midlatitudes and that the agreement between datasets is greatest in the tropics. Thus, studies restricted to low latitudes may reveal more robust trends in the observational datasets.

Our study indicates that a multivariate fingerprint that captures coherent changes across multiple variables may yield shorter detection times. Further work may incorporate other cloud properties such as optical depth or liquid water path that may have robust responses to anthropogenic forcing and can be observed from space.

Using these indicators, we identified robust patterns characteristic of externally forced changes to each indicator. These univariate fingerprints show that models generally predict poleward shifts in the major latitudinal features of total cloud fraction, an increase in total cloud fraction in the tropics and storm tracks and a decrease in the NH subtropics, and a global rise in high cloud. We then combined these indicators to construct a multivariate fingerprint that captures variation between and among the three properties measured. Using multiple indicators resulted in a decreased detection time, with

the model-expected signal emerging as early as 2010. However, we find that multimodel average detection times are not equal across the three indicators. Our results suggest the model-predicted height H signal will emerge earlier than the latitude or total cloud amount signals, although H trends are not significant over the observational period. This is consistent with Bellomo et al. (2014), who found observed trends in regional patterns of cloud cover from ship observations to be of the same sign as model-predicted trends, although model trends over the observed period were not statistically significant.

Applying formal D&A methodology to ISCCP and PATMOS-x observational data does not result in an unambiguous signal detection, but rather yields important insights into areas where the datasets agree and disagree. In particular, ISCCP and PATMOS-x both show a strong trend in the projection onto our L-only fingerprint. This is consistent with previous work (Lucas et al. 2014; Quan et al. 2014; Adam et al. 2014) that has identified strong latitudinal shifts that exceed model predictions in several diagnostic variables (Davis and Rosenlof 2012). The detection and attribution literature also reveals poleward migrations of the Hadley cell edges (Min and Son 2013) and the major features of zonal average precipitation (Marvel and Bonfils 2013) consistent with this picture. The width of the Hadley cell may be affected by external forcing such as ozone depletion (Polvani et al. 2011), black carbon (Allen et al. 2012), and other anthropogenic aerosol emissions (Allen et al. 2014) and is primarily governed by the SST gradient (Adam et al. 2014), which changes under internal variability and external forcing. Our results indicate that useful, consistent trend information can indeed be derived from current satellite-based data and provides more evidence for a discrepancy between modeled and observed changes to the major features of the circulation.

Our work raises several questions, which will guide future work. First, is the observational uncertainty reduced when known spurious trends are removed from the observational datasets? Future work will consider artifact-corrected data (Norris and Evan 2015) and will compare trends in the "raw" data considered here to trends in the corrected datasets. Second, how well do models simulate internal variability? D&A studies rely on models to estimate underlying climate noise and to determine the signal-to-noise ratio; confidence that the amplitude of natural variability is not undersimulated is crucial if we wish to trust these studies. Third, how and why does detection time vary across models? It may be the case that models with differing equilibrium climate sensitivities or transient climate responses to the doubling of atmospheric CO_2 show differing signals in the univariate or multivariate patterns. However, the role of model sensitivity in determining the amplitude or structure of internal variability in cloud properties is relatively understudied. Finally, our fingerprint is derived from CMIP5 historical and RCP8.5 simulations, which are dominated by anthropogenic forcings. However, the observational period includes small changes in solar forcing, along with a large volcanic event (the eruption of Mt. Pinatubo in 1991). Future work is necessary to attribute observed and predicted cloud changes to anthropogenic or natural forcings, as well as to different anthropogenic forcings such as ozone depletion or the emissions of greenhouse gases or tropospheric aerosols.

The results presented in this study support ongoing efforts to improve existing long-term satellite records. By highlighting areas of disagreement, and by showing that the extraction of useful trend information is possible, we provide motivation for continuing study of ISCCP and PATMOS-x. However, we find that multivariate signals of externally forced cloud change are predicted to emerge on relatively short time scales: an encouraging result for planned future missions such as the Climate Absolute Radiance and Refractivity Observatory (CLARREO; Wielicki et al. 2013).

Acknowledgments. CMIP5 data processing was enabled by the CDAT analysis package. The EOF analysis was performed using the eofs software package available from http://ajdawson.github.io/eofs/. This work was supported by the Regional and Global Climate Modeling Program of the U.S. Department of Energy (DOE) Office of Science and was performed under the auspices of the DOE Lawrence Livermore National Laboratory (Contract DE-AC52-07NA27344). KM was supported by a Laboratory Directed Research and Development award (13-ERD-032). CB was supported by the DOE/OBER Early Career Research Program Award SCW1295. We acknowledge the World Climate Research Programme's Working Group on Coupled Modelling, which is responsible for CMIP, and we thank the climate modeling groups (listed in Table A1 of this paper) for producing and making available their model output. For CMIP the U.S. Department of Energy's Program for Climate Model Diagnosis and Intercomparison provides coordinating support and led development of software infrastructure in partnership with the Global Organization for Earth System Science Portals.

APPENDIX A

Model Data

We use model output from phase 5 of the Coupled Model Intercomparison Project (CMIP5; Taylor et al. 2012). All data are available for download via the Earth

TABLE A1. Official acronyms and modeling center information of the CMIP5 models used in this study. (Expansions of model name acronyms are available online at http://www.ametsoc.org/PubsAcronymList.)

Model	Country	Modeling center
ACCESS1.0	Australia	Commonwealth Scientific and Industrial Research Organisation (CSIRO), and Bureau of Meteorology (BoM)
ACCESS1.3	Australia	Commonwealth Scientific and Industrial Research Organisation (CSIRO), and Bureau of Meteorology (BoM)
BCC-CSM1.1	China	Beijing Climate Center (BCC), China Meteorological Administration
BCC-CSM1.1-M	China	Beijing Climate Center (BCC), China Meteorological Administration
BNU-ESM	China	College of Global Change and Earth System Science, Beijing Normal University
CanESM2	Canada	Canadian Centre for Climate Modelling and Analysis
CCSM4	United States	NSF, DOE, and National Center for Atmospheric Research (NCAR), Boulder, Colorado
CESM1(CAM5)–1-FV2	United States	NSF, DOE, and National Center for Atmospheric Research (NCAR), Boulder, Colorado
CESM1(WACCM)	United States	NSF, DOE, and National Center for Atmospheric Research (NCAR), Boulder, Colorado
CMCC-CMS	Italy	Centro Euro-Mediterraneo per i Cambiamenti Climatici (CMCC), Bologna
CNRM-CM5	France	Centre National de Recherches Météorologiques (CNRM), Météo-France, and Centre Européen de Recherches et de Formation Avancée en Calcul Scientifique (CERFACS), Toulouse
CSIRO Mk3.6.0	Australia	Australian Commonwealth Scientific and Industrial Research Organisation (CSIRO) Marine and Atmospheric Research, Melbourne, in collaboration with the Queensland Climate Change Centre of Excellence (QCCCE), Brisbane
EC-EARTH	European Union	EC-Earth Consortium
FGOALS-g2	China	Institute of Atmospheric Physics (IAP), Chinese Academy of Sciences (CAS), Beijing, and Tsinghua University
FGOALS-s2	China	Institute of Atmospheric Physics (IAP), Chinese Academy of Sciences (CAS), Beijing
FIO-ESM	China	First Institute of Oceanography (FIO), State Oceanic Administration (SOA), Qingdao
GFDL CM3	United States	NOAA/GFDL, Princeton, New Jersey
GFDL-ESM2M	United States	NOAA/GFDL, Princeton, New Jersey
GISS-E2-H	United States	NASA Goddard Institute for Space Studies (GISS), New York, New York
GISS-E2-R	United States	NASA Goddard Institute for Space Studies (GISS), New York, New York
HadGEM2-CC	United Kingdom	Met Office Hadley Centre, Exeter (http://www.metoffice.gov.uk)
HadGEM2-ES	United Kingdom	Met Office Hadley Centre, Exeter (http://www.metoffice.gov.uk)
IPSL-CM5A-LR	France	L'Institut Pierre Simon Laplace (IPSL), Paris
IPSL-CM5A-MR	France	L'Institut Pierre Simon Laplace (IPSL), Paris
IPSL-CM5B-LR	France	L'Institut Pierre Simon Laplace (IPSL), Paris
MIROC-ESM	Japan	Japan Agency for Marine-Earth Science and Technology (JAMSTEC), Kanagawa, Atmosphere and Ocean Research Institute (AORI), The University of Tokyo, Chiba, and National Institute for Environmental Studies (NIES), Ibaraki
MIROC-ESM-CHEM	Japan	Japan Agency for Marine-Earth Science and Technology (JAMSTEC), Kanagawa, Atmosphere and Ocean Research Institute (AORI), The University of Tokyo, Chiba, and National Institute for Environmental Studies (NIES), Ibaraki
MIROC5	Japan	Atmosphere and Ocean Research Institute (AORI), The University of Tokyo, Chiba, National Institute for Environmental Studies (NIES), Ibaraki, and Japan Agency for Marine-Earth Science and Technology (JAMSTEC), Kanagawa
MPI-ESM-LR	Germany	Max Planck Institute for Meteorology
MPI-ESM-MR	Germany	Max Planck Institute for Meteorology
MPI-ESM-P	Germany	Max Planck Institute for Meteorology
MRI-CGCM3	Japan	Meteorological Research Institute (MRI), Tsukuba
NorESM1-M	Norway	Norwegian Climate Centre
NorESM1-ME	Norway	Norwegian Climate Centre

TABLE A2. CMIP5 historical and RCP8.5 simulations used in this study, with their tracking IDs.

Model	EM	Tracking ID (historical)	Tracking ID (RCP8.5)
ACCESS1.0	r1i1p1	07cc4198–3b18–442e-878a-00d7c8483c8b	56184ffb-a040–4808–8232-a8378233e17e
ACCESS1.3	r1i1p1	3d81c1bc-c025–4d77–8add-284a51e53c09	3234b999–0748–4c66–8927-cf8cc89f37d7
BNU-ESM	r1i1p1	1b040afc-6f9c-4df0-b5e1–4177f19c35e9	d1da0098–54bc-433a-a903–8ca448c8ef56
CCSM4	r6i1p1	eee235fe-e187–4294-bd62–47cfb30ef6dc	c9eb13f7-afac-4ece-bd92-efc0e0ebd317
CCSM4	r1i1p1	c8cb47c1-f7bd-438f-90f2-bf22f98165ca	b2970ac9–9a96–495f-8e12–471b666aa066
CCSM4	r2i1p1	de28ae8b-5cb0–4095-b592-dbae0feb14fd	03d9022e-bb7a-4da1–8325–1b691233f0e2
CESM1(CAM5)	r1i1p1	35eef327–3456–4d80-a1a2-edda919d57d3	0e476841–2b58–43ec-972a-de46dc585707
CESM1(CAM5)	r2i1p1	3e3e9a33–3e56–4bf2–8565–8a81e478d129	8177b544-a4dd-4c10-b415–19e2a4d248d0
CESM1(CAM5)	r3i1p1	1ac5d672-c228–4cf3–8f6e-50cfb3b97a43	61a92830–3674–4e2f-b335–7d071225a7fc
CSIRO Mk3.6.0	r8i1p1	cfeb53f2-dfa4–4b4a-ab5e-4ca2d4d4e23f	d82adc46-e9a1–416f-b9b8–75f0499d3d3e
CSIRO Mk3.6.0	r3i1p1	9c2c11ad-e83d-40ad-b1be-a24f3be21951	f7621835–34f7–4f7e-b141-d0bf541287f1
CSIRO Mk3.6.0	r2i1p1	99ff1ca5–3b74–4ac8-b4ef-6b7a674ead99	66aa656b-86d9–4015–88da-06612d7d2c6f
CSIRO Mk3.6.0	r7i1p1	a99200c6–457f-4d04–8c5a-a5570dd6bd9e	7a132928–519c-458c-abe4-e4abec9e354b
CSIRO Mk3.6.0	r5i1p1	7486f9aa-df58–438b-86da-d96ffa44b998	065a25b7–2589–499a-9048–8c810c2ff680
CSIRO Mk3.6.0	r1i1p1	d947aa41–6e68–45d7-acac-8079fc080d03	c0201043–4333–43a3-b03a-3fd625e778a2
CSIRO Mk3.6.0	r10i1p1	c4f50cb9-bcbc-4761–90db-1df2dfee8dbd	f2fb218f-906d-4fc6-ba61–1f32a5d38536
CSIRO Mk3.6.0	r4i1p1	fa9cbe73–56c7–4666-a56f-6ef8564ca895	79cf2399-ad2a-4a6c-943e-14c5970920a7
CSIRO Mk3.6.0	r9i1p1	262cc548–80f8–42dd-8c16–87d8ea2c6bba	8ac24227–4dd1–472c-83bf-b2a3d621b755
CSIRO Mk3.6.0	r6i1p1	98b30a21–4b5c-4f15–9c67–4082092050f6	43e47dcd-640c-442d-9e33–5b7341b3b166
CanESM2	r1i1p1	2df1c4ad-343f-46e1–96e7–3167d84b817c	5442b468-b1e7–4c6b-80bb-0ddc076b791c
CanESM2	r5i1p1	d0b8b532–1265–4f77-ae9f-fe1afa871d93	beb43e50–155e-4ae9–8b36-eb705ee25298
CanESM2	r4i1p1	724f6df4–6da6–4495–8fe4–44599e4840b4	4f466345–303a-4b06-b194-c2eee0b1ac71
CanESM2	r3i1p1	83b128d5–29f3–41cd-9da5–46d852e15f6a	2461bd03-ab25–425d-a81b-a6424d861cbd
CanESM2	r2i1p1	37be7fdc-eb55–4ffa-86ff-95e9b4845a23	12aa33bf-360b-4a3c-a855–973f33fadd86
FIO-ESM	r2i1p1	0826ea58–82ee-4132-bb62–229888510ddb	c1540d5c-6419–44ae-ae08–3ed65aa00aaf
FIO-ESM	r3i1p1	b549d654–02b6–4a2b-baf1–3267255c8f7e	c22d3392-db5d-47ec-8794-f558899a9a86
FIO-ESM	r1i1p1	d64d596f-808f-45bf-8296–32e7885e40a5	8ef2d106–4e8e-4c18-bbda-3387e7a15c8b
GISS-E2-H	r1i1p1	845fee88–5c0d-42f0-ba0b-7f18b599aafe	0fb02189–6bee-46c6–8dea-faa2eb22d086
GISS-E2-H-CC	r1i1p1	005af1c0-d53e-4f5b-960d-f8df902b8c20	56376f9b-cb71–40c9-a239–54e213f74a3b
GISS-E2-R	r1i1p1	706ad5e5-ed2c-46bd-9516-a0e918f8c08c	84646c9b-d664–4ad6-acae-3c5bc902e1f8
GISS-E2-R-CC	r1i1p1	c641b9ff-2c30–482c-9507–684e0e8872ba	f0b72f30–97c3–4ed2-b0a7–307fca540ee8
HadGEM2-CC	r1i1p1	82204e34–95a3–460f-a6e2–73132fb6b84a	2599a217-edc3–4366-ac44-fd155154eba0
HadGEM2-ES	r4i1p1	fd53b119–2d73–4e92–8eb3–60cf0048a30c	b93a15dd-5926–4704-a336–977d7a81e69f
HadGEM2-ES	r2i1p1	40febdb8–89c3–4223–8d59-b7f394f77319	6978cbf6–3eaa-4ebb-b42a-85044e67d830
IPSL-CM5A-LR	r3i1p1	5c88d37c-b9cf-4b6e-95cc-c7ea3791f435	bbfc4f16-cc35–45d4–922e-4de0bf313bd2
IPSL-CM5A-LR	r2i1p1	e9c4f130-cf25–44fd-b703–746f63267f8a	aa0b2f53–48cb-44fc-94db-ed35634aaae7
IPSL-CM5A-LR	r4i1p1	25b29b55–795a-49ea-b598–7349e3c62862	c8d8e363–26f8–41c3–8837–78badfac6eea
IPSL-CM5A-LR	r1i1p1	aa67f13a-c715–496d-aecd-e38d5638c5f8	62216563-b6af-410c-8370–9a1073b0b92b
IPSL-CM5A-MR	r1i1p1	f7bc4758-f7f0–4fa5–9499–8318a5927e52	6785a7ad-9831–4a1d-8866–3f0fefe076fb
IPSL-CM5B-LR	r1i1p1	1e03a655-c3b9–4711–923d-6ce7168a093a	d9fc377b-e172–4264–9f46–1ecbeb940e1a
MIROC-ESM	r1i1p1	79c76029–2052–4649-b49b-ff358acc01b9	ce97b1e9–1fce-4875–99f6–43dcd0f9f91d
MIROC-ESM-CHEM	r1i1p1	6e7bd582–5a27–4c35–83a0–8a864ad68bb8	566ccd86-aab3–4f9c-b7f8–1fe14932dc9f
MIROC5	r3i1p1	bd1809ef-2764–4088–9d7f-4bf913e56216	a92a05fe-f4c9–4511-b4ab-a9df33e65402
MIROC5	r1i1p1	aa74f88c-2bb5–4fcb-9d7c-783fb3e593f7	589be518–8e9a-4733-abf8-d50ecbc7c7e5
MIROC5	r2i1p1	d86f27d8–5680–46f2–9209–243d5c33d087	21173ca3–4c02–4e58–8f90–0815711d5037
MPI-ESM-LR	r2i1p1	19956499–5ac2–4651-ae2d-7fbe63db0ca9	e2240ab7–5efe-4a7f-8db9–791b133d7ef6
MPI-ESM-LR	r1i1p1	12e33eea-ce66–4339–9716–2111ea20d89e	addae416-bf2a-480c-a6aa-eaac68b2deaa
MPI-ESM-LR	r3i1p1	9de44f96–931b-4634–812d-affde6e85e1f	fd783166-c28e-4e89–8bbd-71030d1e0fb6
MPI-ESM-MR	r1i1p1	067abb42–5677–4834-b6b2-abf5c5b42dbd	2d0aa880-fb46–47eb-8c36–679e19be31a2
MRI-CGCM3	r1i1p1	dcfcecd5–7743–4368–98cd-94f4d2b52cf1	51f46dfb-b9bf-4a13-a1f3-bb80c028dca4
NorESM1-M	r1i1p1	d52fcaf2-e063–4a1a-b95d-9c294a5b0cec	135123c9–10b4–46d5-a272-e47ec37cb7c9
NorESM1-ME	r1i1p1	b710e60f-8c76–46f6-ad35-ace4aac731c8	455f89da-f438–4b4e-bf86–78fa08ced19a
BCC-CSM1.1	r1i1p1	c988e4b8-e9bf-454a-bd61-d9b63109c921	87d68a6f-2684–41de-af8d-81a834ca60d5
BCC-CSM1.1-M	r1i1p1	d164ac2d-a51c-449f-a583–6859f7bc99be	21f14252–533a-416d-9bee-b7fa98d1adc2

System Grid (see http://cmip-pcmdi.llnl.gov for further information). Table A1 lists the official acronyms and modeling center information for all models used in this study. The following CMIP5 experiments are used:

Historical simulations with estimated changes in anthropogenic and natural forcings over the period 1850–2005. Because not all models start in 1850, we use data over the period 1900–2005.

TABLE A3. CMIP5 preindustrial control simulations.

Model	EM	Tracking ID	Control run length (months)
ACCESS1.0	r1i1p1	0c065cf1–6c81–4a83-a45d-1e13f369f966	6000
ACCESS1.3	r1i1p1	2c89e8e8–2b3d-4583-b6cd-b1875d27dc4d	6000
BNU-ESM	r1i1p1	9b5a570b-5901–4b36–9349–6ebb4507c258	6708
CCSM4	r1i1p1	bdb87549-ca51–416e-8caa-aecf10f4d6ae	12 612
CESM1(BGC)	r1i1p1	271aefea-3f97–455f-8a6a-d9ecec96f645	6000
CESM1(CAM5)	r1i1p1	4bb892de-4446–4c93-a1c2–652c62848b8f	3828
CESM1(FASTCHEM)	r1i1p1	81535be4–714d-4283-a931–2e3fca062d57	2664
CESM1(WACCM)	r1i1p1	5f37abfd-7096–4d19-bc4f-cfb707f6446a	2400
CSIRO Mk3.6.0	r1i1p1	a6ba79f2-fc43–4bda-bef8–3b7fd916ba7a	6000
CanESM2	r1i1p1	2ae535c3-e293–48f0–9994–6904699963fa	11 952
FIO-ESM	r1i1p1	9ecd9564-fb75–41cf-9aea-06f70b45fed9	9600
GFDL CM3	r1i1p1	5793a2ef-6ab9–414d-a264–44a260e2a608	6000
GFDL-ESM2G	r1i1p1	4d7efe9c-534e-4900–81e0-c1a0cd6e862d	6000
GFDL-ESM2M	r1i1p1	f4aaa9c0-ae2c-4953-bcb1-d5b332a80d48	6000
GISS-E2-H	r1i1p1	eb36f5c6–480f-4bb0–80b5–47b1cd36a0f5	9360
GISS-E2-H-CC	r1i1p1	a2d519a2–27bd-49d1–853e-5ce5c9d9a746	3012
GISS-E2-R	r1i1p1	67b127d9–9545–467a-b13f-25198e099fad	1200
GISS-E2-R-CC	r1i1p1	828e1d58-b7bd-4111–9bc4-d1fd604fa2fd	3012
HadGEM2-CC	r1i1p1	edca00c5–36f6–49e4-bb20–0ed673d1bacf	2881
IPSL-CM5A-LR	r1i1p1	10cdc455-d825–44f3-bef8-d2a97eae9c23	12 000
IPSL-CM5A-MR	r1i1p1	abe410cd-c539–45df-9a83–106bc64f45be	3600
IPSL-CM5B-LR	r1i1p1	668308bb-2205–4132–8a75-cb6a7716c744	3600
MIROC-ESM	r1i1p1	16ba40d8–3532–4abf-b346–66c09f2efa90	7560
MIROC-ESM-CHEM	r1i1p1	375ce3c6–4a26–448d-b0cf-bd57004a995c	3060
MIROC5	r1i1p1	8c59969d-e245–4852–8e54–2c90de6f2961	8040
MPI-ESM-LR	r1i1p1	92c55a3c-2086–407f-a759–9f0c5cc8bacd	12 000
MPI-ESM-MR	r1i1p1	ae44c27e-395d-4890–8da6–54215626027b	12 000
MPI-ESM-P	r1i1p1	a619277a-6763–43e9-a4a1–84ce746f8d23	13 872
MRI-CGCM3	r1i1p1	6787659a-2400–463c-a4f6-ec623991ca16	6000
NorESM1-M	r1i1p1	a6a2cbdd-d01b-4337–8707-e58b299a6963	6012
NorESM1-ME	r1i1p1	18d58b18–80c4–4c65-b8d8-d831d72f7ac4	3024
BCC-CSM1.1	r1i1p1	e6be09df-1cb7–4c9f-841f-dc4c56700071	6000
BCC-CSM1.1-M	r1i1p1	a419cc89-c6b0–41a1-be2e-eba830c20262	4800
INM CM4	r1i1p1	9a7cbe25–70dd-4ab2–98d7–32cf7b40a167	6000

RCP8.5 simulations in which twenty-first-century changes in greenhouse gases and anthropogenic aerosols are prescribed according to representative concentration pathway 8.5 (van Vuuren et al. 2011), generally over the period 2005–2100.

piControl simulations: preindustrial runs with no changes in external climate forcings.

1pctCO2 simulations: runs in which CO_2 is increased at 1% per year for 140 years.

Models with known problems (see http://cmip-pcmdi.llnl.gov/cmip5/errata/cmip5errata.html) are excluded: CMCC models are removed because of errors in vertical coordinates, and FGOALS models are removed because of a number of problems including data corruption, omission of volcanic forcing in the historical experiments, and missing RCP8.5 scenarios. To prevent overdependence on models from NASA's Goddard Institute for Space Studies, we considered only physics version 1 of the GISS-E2-H and GISS-E2-R models. However, because these models fail the five-extrema test, data from these models do not contribute to our results. Tables A2 and A3 list the CMIP5 historical, RCP8.5, 1pctCO2, and piControl simulations used, along with the unique tracking identifier (ID) found in the metadata.

Splicing of historical and future simulations

For extended analysis, CMIP5 historical simulations are combined with RCP8.5 runs to create the ALL+8.5 simulations used in this paper. Model metadata are checked and a spliced file is created provided that

- the designated parent experiment of the RCP8.5 simulation is "historical,"
- the ensemble member (EM) identifiers (as defined in the CMIP5 Data Reference Syntax Document) of the RCP8.5 run and indicated parent match,
- historical experiments end in December 2005 (November 2005 for Hadley Centre models), and

- RCP8.5 experiments begin January 2006 (December 2005 for Hadley Centre models).

Imposing these criteria excludes several available models from the splicing process; those considered for use in this study are listed in Table A2.

APPENDIX B

Observational Datasets

a. ISCCP

The International Satellite Cloud Climatology Project (ISCCP; Rossow and Schiffer 1991, 1999) provides estimates of the area coverage of clouds stratified by the apparent cloud-top pressure of the highest cloud in a column and by the column integrated optical thickness of clouds. These estimates are the results of retrieval algorithms applied to radiance observations from the visible and infrared window channels of geostationary and polar-orbiting satellites. In the retrieval algorithm, scenes are classified as cloudy if the visible or infrared radiance in the 1–5-km field of view differs from the clear-sky value by more than the detection threshold. Optical thickness and cloud-top temperature are computed for each cloudy scene by comparing the observed visible or infrared radiance with that computed from a radiative transfer model, and a temperature profile from the TIROS Operational Vertical Sounder is used to convert cloud-top temperature to cloud-top pressure. These data are accumulated for 280 km × 280 km regions every 3 h starting in July 1983.

In this study we make use of the GCM simulator-oriented ISCCP cloud product, which is constructed from daytime-only monthly averages of the ISCCP D1 cloud dataset (Rossow and Schiffer 1999) over the period July 1983–June 2008. Estimates of cloud coverage are provided in a joint histogram with six optical depth bins and seven cloud-top pressure bins. This product is described more fully in Pincus et al. (2012) and is available from http://climserv.ipsl.polytechnique.fr/cfmip-obs/.

Vertical profiles of cloud fraction are computed by summing the joint histograms over all optical depths. Total cloud fraction is computed by summing over all bins of the histogram.

b. PATMOS-x

The Pathfinder Atmospheres-Extended (PATMOS-x) dataset is derived from measurements from all five channels of NOAA's Advanced Very High Resolution Radiometer (AVHRR) sensor on board the polar-orbiting platforms of NOAA and EUMETSAT. Cloud detection is based on six Bayesian classifiers computed separately for seven surface types. These Bayesian classifiers were derived through the objective analysis of collocated AVHRR observations from *NOAA-18* and Cloud–Aerosol Lidar with Orthogonal Polarization (CALIOP) observations from *Cloud–Aerosol Lidar and Infrared Pathfinder Satellite Observations* (*CALIPSO*) (Heidinger et al. 2012). Retrievals of cloud temperature and cloud emissivity are based on an optimal estimation approach applied to AVHRR split-window observations (Heidinger and Pavolonis 2009).

Here we make use of PATMOS-x data between January of 1982 and December of 2009 that is provided by the GEWEX Cloud Assessment (Stubenrauch et al. 2013). Total cloud fraction estimates from up to four local observation times are averaged together in generating the monthly-mean total cloud amounts used in this study. For vertically resolved cloud fraction information, we use joint histograms of cloud fraction segregated into seven cloud-top pressure bins and five cloud infrared emissivity bins. These are taken from the 1330 local time retrievals, and we sum them over all cloud emissivity bins. The PATMOS-x data are available from http://climserv.ipsl.polytechnique.fr/gewexca/.

REFERENCES

Adam, O., T. Schneider, and N. Harnik, 2014: Role of changes in mean temperatures versus temperature gradients in the recent widening of the Hadley circulation. *J. Climate,* **27,** 7450–7461, doi:10.1175/JCLI-D-14-00140.1.

Allen, M., and P. Stott, 2003: Estimating signal amplitudes in optimal fingerprinting, part I: Theory. *Climate Dyn.,* **21,** 477–491, doi:10.1007/s00382-003-0313-9.

Allen, R. J., S. C. Sherwood, J. R. Norris, and C. S. Zender, 2012: Recent northern hemisphere tropical expansion primarily driven by black carbon and tropospheric ozone. *Nature,* **485,** 350–354, doi:10.1038/nature11097.

——, J. R. Norris, and M. Kovilakam, 2014: Influence of anthropogenic aerosols and the Pacific decadal oscillation on tropical belt width. *Nat. Geosci.,* **7,** 270–274, doi:10.1038/ngeo2091.

Andrews, T., J. M. Gregory, M. J. Webb, and K. E. Taylor, 2012: Forcing, feedbacks and climate sensitivity in CMIP5 coupled atmosphere–ocean climate models. *Geophys. Res. Lett.,* **39,** L09712, doi:10.1029/2012GL051607.

Barnett, T. P., and Coauthors, 2008: Human-induced changes in the hydrology of the western United States. *Science,* **319,** 1080–1083, 10.1126/science.1152538.

Bellomo, K., A. C. Clement, J. R. Norris, and B. J. Soden, 2014: Observational and model estimates of cloud amount feedback over the Indian and Pacific Oceans. *J. Climate,* **27,** 925–940, doi:10.1175/JCLI-D-13-00165.1.

Bender, F. A., V. Ramanathan, and G. Tselioudis, 2012: Changes in extratropical storm track cloudiness 1983–2008: Observational support for a poleward shift. *Climate Dyn.,* **38,** 2037–2053, doi:10.1007/s00382-011-1065-6.

Bony, S., and Coauthors, 2006: How well do we understand and evaluate climate change feedback processes? *J. Climate,* **19,** 3445–3482, doi:10.1175/JCLI3819.1.

Ceppi, P., M. D. Zelinka, and D. L. Hartmann, 2014: The response of the Southern Hemispheric eddy-driven jet to future changes in shortwave radiation in CMIP5. *Geophys. Res. Lett.,* **41,** 3244–3250, doi:10.1002/2014GL060043.

Davis, S. M., and K. H. Rosenlof, 2012: A multidiagnostic intercomparison of tropical-width time series using reanalyses and satellite observations. *J. Climate,* **25,** 1061–1078, doi:10.1175/JCLI-D-11-00127.1.

Deser, C., and J. M. Wallace, 1990: Large-scale atmospheric circulation features of warm and cold episodes in the tropical Pacific. *J. Climate,* **3,** 1254–1281, doi:10.1175/1520-0442(1990)003<1254:LSACFO>2.0.CO;2.

Eastman, R., S. G. Warren, and C. J. Hahn, 2011: Variations in cloud cover and cloud types over the ocean from surface observations, 1954–2008. *J. Climate,* **24,** 5914–5934, doi:10.1175/2011JCLI3972.1.

Evan, A. T., A. K. Heidinger, and D. J. Vimont, 2007: Arguments against a physical long-term trend in global ISCCP cloud amounts. *Geophys. Res. Lett.,* **34,** L04701, doi:10.1029/2006GL028083.

Gillett, N., F. Zwiers, A. Weaver, G. Hegerl, M. Allen, and P. Stott, 2002: Detecting anthropogenic influence with a multi-model ensemble. *Geophys. Res. Lett.,* **29,** 1970, doi:10.1029/2002GL015836.

Grise, K. M., and L. M. Polvani, 2014: Southern Hemisphere cloud–dynamics biases in CMIP5 models and their implications for climate projections. *J. Climate,* **27,** 6074–6092, doi:10.1175/JCLI-D-14-00113.1.

Hansen, J., A. Lacis, D. Rind, G. Russell, P. Stone, I. Fung, R. Ruedy, and J. Lerner, 1984: Climate sensitivity: Analysis of feedback mechanisms. *Climate Processes and Climate Sensitivity, Geophys. Monogr.,* Vol. 29, Amer. Geophys. Union, 130–163.

Hartmann, D. L., and K. Larson, 2002: An important constraint on tropical cloud–climate feedback. *Geophys. Res. Lett.,* **29,** 1951, doi:10.1029/2002GL015835.

Hasselmann, K., 1979: On the signal-to-noise problem in atmospheric response studies. *Meteorology of Tropical Oceans,* D. B. Shaw, Ed., Royal Meteorological Society, 251–259.

Hawkins, E., and R. Sutton, 2012: Time of emergence of climate signals. *Geophys. Res. Lett.,* **39,** L01702, doi:10.1029/2011GL050087.

Hegerl, G. C., H. von Storch, K. Hasselmann, B. D. Santer, U. Cubasch, and P. D. Jones, 1996: Detecting greenhouse-gas-induced climate change with an optimal fingerprint method. *J. Climate,* **9,** 2281–2306, doi:10.1175/1520-0442(1996)009<2281:DGGICC>2.0.CO;2.

Heidinger, A. K., and M. J. Pavolonis, 2009: Gazing at cirrus clouds for 25 years through a split window. Part I: Methodology. *J. Appl. Meteor. Climatol.,* **48,** 1100–1116, doi:10.1175/2008JAMC1882.1.

——, A. T. Evan, M. J. Foster, and A. Walther, 2012: A naive Bayesian cloud-detection scheme derived from *CALIPSO* and applied within PATMOS-x. *J. Appl. Meteor. Climatol.,* **51,** 1129–1144, doi:10.1175/JAMC-D-11-02.1.

——, M. J. Foster, A. Walther, and X. Zhao, 2014: The Pathfinder Atmospheres–Extended AVHRR climate dataset. *Bull. Amer. Meteor. Soc.,* **95,** 909–922, doi:10.1175/BAMS-D-12-00246.1.

Held, I. M., and B. J. Soden, 2006: Robust responses of the hydrological cycle to global warming. *J. Climate,* **19,** 5686–5699, doi:10.1175/JCLI3990.1.

Johanson, C. M., and Q. Fu, 2009: Hadley cell widening: Model simulations versus observations. *J. Climate,* **22,** 2713–2725, doi:10.1175/2008JCLI2620.1.

Kay, J., B. Medeiros, Y.-T. Hwang, A. Gettelman, J. Perket, and M. Flanner, 2014: Processes controlling Southern Ocean shortwave climate feedbacks in CESM. *Geophys. Res. Lett.,* **41,** 616–622, doi:10.1002/2013GL058315.

Klein, S. A., and C. Jakob, 1999: Validation and sensitivities of frontal clouds simulated by the ECMWF model. *Mon. Wea. Rev.,* **127,** 2514–2531, doi:10.1175/1520-0493(1999)127<2514:VASOFC>2.0.CO;2.

Levy, A. A., W. Ingram, M. Jenkinson, C. Huntingford, F. H. Lambert, and M. Allen, 2013: Can correcting feature location in simulated mean climate improve agreement on projected changes? *Geophys. Res. Lett.,* **40,** 354–358, doi:10.1002/2012GL053964.

——, M. Jenkinson, W. Ingram, F. H. Lambert, C. Huntingford, and M. Allen, 2014: Increasing the detectability of external influence on precipitation by correcting feature location in GCMs. *J. Geophys. Res. Atmos.,* **119,** 12 466–12 478, doi:10.1002/2014JD02235.

Loeb, N. G., and Coauthors, 2007: Multi-instrument comparison of top-of-atmosphere reflected solar radiation. *J. Climate,* **20,** 575–591, doi:10.1175/JCLI4018.1.

Lu, J., G. Chen, and D. M. Frierson, 2008: Response of the zonal mean atmospheric circulation to El Niño versus global warming. *J. Climate,* **21,** 5835–5851, doi:10.1175/2008JCLI2200.1.

Lucas, C., B. Timbal, and H. Nguyen, 2014: The expanding tropics: A critical assessment of the observational and modeling studies. *Wiley Interdiscip. Rev.: Climate Change,* **5,** 89–112, doi:10.1002/wcc.251.

Mahlstein, I., R. Knutti, S. Solomon, and R. Portmann, 2011: Early onset of significant local warming in low latitude countries. *Environ. Res. Lett.,* **6,** 034009, doi:10.1088/1748-9326/6/3/034009.

Marvel, K., and C. Bonfils, 2013: Identifying external influences on global precipitation. *Proc. Natl. Acad. Sci. USA,* **110,** 19 301–19 306, doi:10.1073/pnas.1314382110.

Min, S.-K., and S.-W. Son, 2013: Multi-model attribution of the Southern Hemisphere Hadley cell widening: Major role of ozone depletion. *J. Geophys. Res. Atmos.,* **118,** 3007–3015, doi:10.1002/jgrd.50232.

Norris, J. R., 1999: On trends and possible artifacts in global ocean cloud cover between 1952 and 1995. *J. Climate,* **12,** 1864–1870, doi:10.1175/1520-0442(1999)012<1864:OTAPAI>2.0.CO;2.

——, 2007: Observed interdecadal changes in cloudiness: Real or spurious? *Climate Variability and Extremes during the Past 100 Years,* S. Brönnimann et al., Eds., Springer, 169–178.

——, and A. T. Evan, 2015: Empirical removal of artifacts from the ISCCP and PATMOS-x satellite cloud records. *J. Atmos. Oceanic Technol.,* doi:10.1175/JTECH-D-14-00058.1, in press.

Pincus, R., S. Platnick, S. A. Ackerman, R. S. Hemler, and R. J. Patrick Hofmann, 2012: Reconciling simulated and observed views of clouds: MODIS, ISCCP, and the limits of instrument simulators. *J. Climate,* **25,** 4699–4720, doi:10.1175/JCLI-D-11-00267.1.

Polvani, L. M., D. W. Waugh, G. J. Correa, and S.-W. Son, 2011: Stratospheric ozone depletion: The main driver of twentieth-century atmospheric circulation changes in the Southern Hemisphere. *J. Climate,* **24,** 795–812, doi:10.1175/2010JCLI3772.1.

Quan, X.-W., M. P. Hoerling, J. Perlwitz, H. F. Diaz, and T. Xu, 2014: How fast are the tropics expanding? *J. Climate,* **27,** 1999–2013, doi:10.1175/JCLI-D-13-00287.1.

Rossow, W. B., and R. A. Schiffer, 1991: ISCCP cloud data products. *Bull. Amer. Meteor. Soc.,* **72,** 2–20, doi:10.1175/1520-0477(1991)072<0002:ICDP>2.0.CO;2.

——, and ——, 1999: Advances in understanding clouds from ISCCP. *Bull. Amer. Meteor. Soc.,* **80,** 2261–2287, doi:10.1175/1520-0477(1999)080<2261:AIUCFI>2.0.CO;2.

Santer, B. D., U. Mikolajewicz, W. Brüggemann, U. Cubasch, K. Hasselmann, H. Höck, E. Maier-Reimer, and T. M. Wigley, 1995: Ocean variability and its influence on the detectability of greenhouse warming signals. *J. Geophys. Res.,* **100,** 10 693–10 725, doi:10.1029/95JC00683.

——, and Coauthors, 2003: Contributions of anthropogenic and natural forcing to recent tropopause height changes. *Science,* **301,** 479–483, doi:10.1126/science.1084123.

——, and Coauthors, 2007: Identification of human-induced changes in atmospheric moisture content. *Proc. Natl. Acad. Sci. USA,* **104,** 15 248–15 253, doi:10.1073/pnas.0702872104.

——, and Coauthors, 2013: Identifying human influences on atmospheric temperature. *Proc. Natl. Acad. Sci. USA,* **110,** 26–33, doi:10.1073/pnas.1210514109.

Scheff, J., and D. Frierson, 2012: Twenty-first-century multimodel subtropical precipitation declines are mostly midlatitude shifts. *J. Climate,* **25,** 4330–4347, doi:10.1175/JCLI-D-11-00393.1.

Seidel, D. J., Q. Fu, W. J. Randel, and T. J. Reichler, 2008: Widening of the tropical belt in a changing climate. *Nat. Geosci.,* **1,** 21–24, doi:10.1038/ngeo.2007.38.

Singh, M. S., and P. A. O'Gorman, 2012: Upward shift of the atmospheric general circulation under global warming: Theory and simulations. *J. Climate,* **25,** 8259–8276, doi:10.1175/JCLI-D-11-00699.1.

Stephens, G. L., 2005: Cloud feedbacks in the climate system: A critical review. *J. Climate,* **18,** 237–273, doi:10.1175/JCLI-3243.1.

Stott, P. A., S. Tett, G. Jones, M. Allen, J. Mitchell, and G. Jenkins, 2000: External control of 20th century temperature by natural and anthropogenic forcings. *Science,* **290,** 2133–2137, doi:10.1126/science.290.5499.2133.

Stubenrauch, C., and Coauthors, 2013: Assessment of global cloud datasets from satellites: Project and database initiated by the GEWEX radiation panel. *Bull. Amer. Meteor. Soc.,* **94,** 1031–1049, doi:10.1175/BAMS-D-12-00117.1.

Taylor, K. E., R. J. Stouffer, and G. A. Meehl, 2012: An overview of CMIP5 and the experiment design. *Bull. Amer. Meteor. Soc.,* **93,** 485–498, doi:10.1175/BAMS-D-11-00094.1.

Tett, S. F., and Coauthors, 2002: Estimation of natural and anthropogenic contributions to twentieth century temperature change. *J. Geophys. Res.,* **107,** 4306, doi:10.1029/2000JD000028.

Tian, L., and J. A. Curry, 1989: Cloud overlap statistics. *J. Geophys. Res.,* **94,** 9925–9935, doi:10.1029/JD094iD07p09925.

van Vuuren, D. P., and Coauthors, 2011: The representative concentration pathways: An overview. *Climatic Change,* **109,** 5–31, doi:10.1007/s10584-011-0148-z.

Vial, J., J.-L. Dufresne, and S. Bony, 2013: On the interpretation of inter-model spread in CMIP5 climate sensitivity estimates. *Climate Dyn.,* **41,** 3339–3362, doi:10.1007/s00382-013-1725-9.

Weatherhead, E. C., and Coauthors, 1998: Factors affecting the detection of trends: Statistical considerations and applications to environmental data. *J. Geophys. Res.,* **103,** 17 149–17 161, doi:10.1029/98JD00995.

Webb, M., C. Senior, S. Bony, and J.-J. Morcrette, 2001: Combining ERBE and ISCCP data to assess clouds in the Hadley Centre, ECMWF and LMD atmospheric climate models. *Climate Dyn.,* **17,** 905–922, doi:10.1007/s003820100157.

Wetherald, R., and S. Manabe, 1988: Cloud feedback processes in a general circulation model. *J. Atmos. Sci.,* **45,** 1397–1416, doi:10.1175/1520-0469(1988)045<1397:CFPIAG>2.0.CO;2.

Wielicki, B. A., and Coauthors, 2013: Achieving climate change absolute accuracy in orbit. *Bull. Amer. Meteor. Soc.,* **94,** 1519–1539, doi:10.1175/BAMS-D-12-00149.1.

Yin, J. H., 2005: A consistent poleward shift of the storm tracks in simulations of 21st century climate. *Geophys. Res. Lett.,* **32,** L18701, doi:10.1029/2005GL023684.

Zelinka, M. D., and D. L. Hartmann, 2011: The observed sensitivity of high clouds to mean surface temperature anomalies in the tropics. *J. Geophys. Res.,* **116,** D23103, doi:10.1029/2011JD016459.

——, S. A. Klein, K. E. Taylor, T. Andrews, M. J. Webb, J. M. Gregory, and P. M. Forster, 2013: Contributions of different cloud types to feedbacks and rapid adjustments in CMIP5. *J. Climate,* **26,** 5007–5027, doi:10.1175/JCLI-D-12-00555.1.